Steady Heat Transfer Predictions For A Highly Loaded Single Stage Turbine With Flat Tip

A Thesis
Presented in Partial Fulfillment of the Requirements for
The Degree of Master of Science in the
Graduate School of the Ohio State University

By
Daniel Hung-Fai Luk, B.S.
*****
The Ohio State University
2008

Master's Examination Committee:
Dr. Jen-Ping Chen, Advisor
Dr. Ali Ameri, Advisor
Dr. Mo-How Herman Shen

Approved By:

_____
Advisor

Aeronautical and Astronautical
Engineering Graduate Program

ABSTRACT

This thesis presents steady computational predictions for a single stage (2-blade-row), highly loaded, turbine. Computational predictions and experimental measurements of heat flux are compared for both the stator vane and the rotor blade with a flat tip. Comparisons for both blade rows are presented at three different spanwise locations as well as on the hub and casing endwalls and rotor tip. The experimental measurements were taken from earlier experiments conducted at the Ohio State University Gas Turbine Laboratory Test Facility. The computational predictions were achieved using TURBO. This CFD code is a 3D, Reynolds-Averaged Navier-Stokes (RANS), computational fluid dynamics code capable of handling unsteady flows. The CFD solutions were steady and computed as two separate computations. First, the stator vane simulation was performed using known inlet and exit boundary conditions. Then, inlet boundary conditions for the rotor blade simulation were taken from radial exit profiles of the steady stator vane solution and exit boundary conditions for the rotor blade was taken from previous CFD solutions which involved a 3-blade row simulation. The CFD heat transfer predictions compared well with the stator vane experimental values. The CFD heat flux prediction comparisons with the experimental measurements for the rotor blade were only fair. The largest percent error between the computation

and the experimental measurements was 25%. The predictions for the hub of the rotor blade had good agreement with the experimental data. Most of the predictions were within the tight scatter of experimental data. The CFD heat transfer prediction for the rotor tip had good agreement with previous computational predictions but only fair agreement with experimental data. The rotor tip predictions for heat transfer were on average 15.5% greater than the experimental measurements. The rotor blade casing surface heat transfer results are presented in this thesis, however there were no other data for the results to be compared to. Detailed analysis and discussion over the CFD predictions and results are contained in this thesis.

Dedicated to my parents whose faithful love and patience has allowed me to achieve my goals.

ACKNOWLEDGMENTS

I would like thank my adviser, Dr. Ali Ameri, who has guided me and challenged me so that my understanding of computational fluid dynamics and heat transfer would grow.

I would also like to thank Dr. Jen-Ping Chen, for his work on TURBO, and for all the time he has invested in my education in this field.

I would like to thank Vikram Shyam, for his Preprocessor code, for his tireless efforts to answer all my questions and help me in any way that I needed throughout the entire process of conducting computations and writing the thesis.

I would like to thank Dr. Shen for sitting on my committee.

I would also like to thank my office mates for being great friends and for their input.

I would like to thank the Ohio Super Computer Center for the priority on computational time given to our research group.

VITA

June 30, 1984 . . . . . Born - Cincinnati, Ohio

2006 . . . . . .B.S. Aeronautical and Astronautical Engineering, Ohio State University

2006-present . . . . . Graduate Research Associate - The Ohio State University

FIELDS OF STUDY

Major Field: Aeronautical and Astronautical Engineering

TABLE OF CONTENTS

LIST OF FIGURES

LIST OF TABLES

NOMENCLATURE

a	speed of sound
A	Surface area
c	Sutherland's constant for the gaseous material
c_p	Specific heat at constant pressure
fv	Field view
h	Heat transfer coefficient: $h = \frac{q_{wall}}{T_{wall} - T_{ref}}$
Re	Reynolds Number
Re/L	Reynolds Number per meter length: $Re = \frac{\dot{m}/A_{inlet}}{\mu}$
R	Gas constant for air
γ	Specific heat ratio
$\dot{m}$	Mass flow
Pr	Prandtl number

PR	Pressure Ratio
k	Coefficient of thermal convection
q	Heat flux
S	Surface Distance from the Geometric Leading Edge to the Trailing Edge, at Constant Percent Span, Non-Dimensionalized: (0 to +1 on the Suction Surface, 0 to -1 on the Pressure Surface), $S_2 = \sqrt{(x_2 - x_1)^2 + (y_2 - y_1)^2 + (z_2 - z_1)^2} + S_1$
St	Stanton Number, $St = \frac{q_{wall}}{\left(\frac{\dot{m}}{A}\right) \cdot c_P \cdot \left[T_{wall} - T_{ref}\right]}$
T	Static temperature
$\bar{T}$	Non-Dimensional Temperature
T_0	total stagnation temperature
n	component in the normal direction
u_*	friction velocity
V	Velocity
V_{rel}	Relative velocity
V_{abs}	Absolute Velocity
x,y,z	Cartesian coordinates
y+	non-dimensional wall distance, $y^+ \equiv \frac{u_* y}{\nu}$

α	radial angle
β	tangential angle
ρ	density of fluid
x_0	reference length of blade (maximum diameter of blade tip)
θ	angle in degrees
τ_w	Shear stress
μ	dynamic viscosity coefficient
μ_0	reference dynamic viscosity coefficient
ν	viscosity

subscripts

0	Reference value
wall	at a wall boundary

CHAPTER 1

INTRODUCTION

1.1 General Background

Computational fluid dynamics (CFD) has become an alternative way to wind tunnel testing for predicting and examining the capabilities of aircraft engines. Comparisons of experimental data with computational results help to improve CFD codes. The purpose of this thesis is to compare the results of two computer simulations and experimental results with a focus on the heat transfer on the blade surfaces, end-walls, and rotor blade tip.

Heat transfer is an important design consideration for turbine blades because the current industry trend is to push the turbine inlet temperature higher. There is a lot of emphasis placed on increasing turbine inlet temperature because it directly increases the efficiency and performances of the aircraft engines they are used in. One of the main limiting factors that keep designers from pushing the inlet temperature higher is the material of the turbine blade (Haldeman and Dunn [25]). Another reason for the

study of heat transfer is that accurate predictions lead to enhanced turbine blade design, i.e. film cooling and tip clearance. In film cooling, cool air is bled from the compressor stage, ducted to the internal chambers of the turbine blades, and discharged through small holes in the blade walls. This air provides a thin, cool, insulating blanket along the external surface of the turbine blade. The tips of turbine blades rotate in close proximity to the casing surface. For efficiency in performance, engine designers desire to keep the tip clearance at a minimum. Increased knowledge of the heat transfer in the rotor tip can inform designers the variations in clearance due to thermal expansion (Molter, et al. [28]).

It should be noted that Ameri et al. [8] has found that the unsteady wake has significant effects on the distribution of heat transfer on the blade. The distribution that is obtained from an unsteady computation is different from a steady computation. This paper will present numerical calculations on heat flux over a turbine blade in steady-state conditions. The computational results presented in this thesis will give a better idea of the characteristics and patterns of heat transfer over a turbine blade.

Haldeman [24] obtained experimental and computational results for a fully cooled, high-work single stage high pressure turbine. The effect of rotation on the inner static pressure distribution in the rotor was demonstrated in his paper. Haldeman et al. [23] have also been able to acquire heat-transfer measurements using a modern one and 1/2 stage high-pressure turbine operating at design corrected conditions and pressure ratio. Tallman et al. [34] has done a comparison of computational predictions with the experimental data from Haldeman [24]. Their predictions were obtained from a single computation of a one and one-half stage turbine. His CFD heat transfer predictions compared favorably with the local measurements of heat transfer. The paper

by Molter et al. [28] on heat-flux measurements and predictions involved a modern one-and-one-half stage high-pressure turbine operating at design corrected conditions in a rotating rig. They found that the recessed tip, used to minimize blade damage, increased the heat transfer on the blade and created hot spots on the floor of the recess. They also concluded that steady-state CFD analysis would be useful in predicting heat load distribution in turbine blade tips.

1.2 Rotor Tip

The tips of high-pressure turbine blades rotate at high speeds at a small distance from the outer seal or shroud. Unshrouded blades have a gap between the blade tip and the shroud. The distance between the blade tip and the shroud is called the tip clearance. Some aircraft engine companies use shrouded blades to eliminate the tip rub problem. Tip clearances need to be relatively small for performance reasons. Even small clearances will cause leakage flow which leads to poor aerodynamic performance and poor structural durability (Molter, et al. [28]). Blade tips are one of the regions that are usually susceptible to failure. Two reasons for this are high temperatures and limited cooling (Kwak and Han, [27]). The pressure difference between the pressure and suction surfaces causes leakage flow to accelerate which in turn leads to high thermal loads in the tip gap. This eventually causes the tip gap to grow in size and leads to failure or tip rubbing (Han, [26]). Molter's results indicated that steady-state CFD analysis were able to capture heat transfer contours in turbine blade tips. These simulations could help shape blade designs.

Green [21] showed that there was essentially no difference in pressure along the

surface of the blade when comparing a blade with a recessed tip and a blade with a flat tip. However, heat transfer is the focus of this paper. Heat transfer is much more susceptible to small changes in aerodynamics than the pressure distribution. The grid has a flat tip with a tip clearance of 2.3%, according to the coordinate data, and will be an important component of the simulation that will be a heavy influence on the computational results. The rotor grid used in the computation by Tallman et al. [34] contained a flat tip with a tip gap of 2.1%. A 2.3% tip clearance is quite large comparatively. Most engine designers push for tip clearances of less than 1% or less than 0.5% for efficiency reasons. However, as the tip gap gets smaller, the probability of tip rubbing increases. Ameri et al. [4] has shown that there is a direct positive correlation between heat transfer and enlargement of the clearance gap. The expected thermal load on all heat transfer surfaces is expected to be relatively large compared to blades with a smaller tip clearance. Ameri et al. [1] did an investigation on the heat transfer on a smooth tip, 2% recess, and a 3% recessed tip, and they reported that the total heat transfer for recessed tips was 80-90 percent higher than that of the flat tips.

The flow field around the tip region is highly three dimensional, time-dependent and complex. The highest and lowest heat loads of the entire blade are found on the rotor tip. Complex flow phenomenon such as shock waves, wakes, separation, reattachment, and vorticies can result in large heat transfer gradients. Molter et al. [28] warns that high heat flux gradients may lead to stresses which lead to blade life reduction.

1.3 Scope of Current Study

The current study covers an aerodynamic study over a 2-blade row turbine. The stator vane is stationary while the rotor blade is rotating counter-clockwise at correct speeds. The rotor blade contains a flat tip. The numerical predictions incorporate the use of computational fluid dynamics code called TURBO. The experimental data was obtained by Haldeman [24] at the Ohio State University Gas Test Facility. The experimental data was obtained using a full-scale rig that included 3-blade rows, a high-pressure turbine (HPT) nozzle, a rotating high-pressure turbine HPT rotor, and a low-pressure turbine (LPT) vane. The rig was operated at proper corrected engine design conditions to match cruise condition for the engine.

First, a three dimensional grid with fine density at all physical boundaries is produced to be used in the MSU-TURBO simulation composed of an upstream 38 vane row with a downstream 72 rotor blade row. A steady-state CFD simulation will be run on the stator vane. Then, the steady rotor blade case will be run with the inlet conditions taken from the steady vane case. This thesis will include the production of the initial mesh for the stator and rotor. This will be done using a grid generation software called GridPro. These simulations will include a $\kappa - \varepsilon$ turbulence model. TURBO will simulate a full annulus with a non-rotating 38 vane stator row and a 72 blade rotor row with tip clearance rotating at 8971 RPM. A comparison of the heat transfer results will be used to validate the accuracy of the computational simulations.

CHAPTER 2

COMPUTATIONAL FLUID DYNAMICS

2.1 Need for CFD

Computer simulated engine tests are becoming very valuable. Experimental tests in the wind tunnel are very expensive compared to the computer simulations. One would then ask why experimental tests are still being conducted if they are so expensive. Computational models for predicting engine tests are still being tested and validated. Also, running CFD simulations can be computationally demanding. OSC (Ohio Supercomputing Center), provides the ability to run TURBO at high speeds in parallel. OSC incorporates the use of MPI, message passing interface, which reduces the turn around time of runs significantly.

One of many disadvantages of an experimental approach is that measurements are physically limited. In the case of turbo-machinery, a limited amount of heat flux gauges can be applied to the surface of a turbine blade. Also, the gauges interfere with the flow-field and causes erroneous results. The CFD approach has the ability

to provide massive amounts of data for analysis, whereas the experimental approach cannot. Experimental tests must account for the pressure and heat-flux gauges used in the experiments which will not be present during actual use.

2.2 Focus of paper

The main objective of this thesis is two-fold. One is to investigate the heat transfer of the rotating rotor blade and compare the predictions with the computation by Tallman et al. [34]. The other is to compare CFD results with experimental results by Haldeman [24] from a rig .

This paper will conduct an examination of a two-blade row case with a focus on the heat transfer on the rotor blade. The numerical results will come from the use of steady CFD predictions. First, the steady state pressure ratios on the surface of the stator vane will be compared with the experimental data from Haldeman [24]. This will give a good indication of whether or not the heat transfer can be compared. Similar studies have been done which show that interaction effects between high-pressure turbine nozzles and high-pressure blades have a small impact on unsteady pressure (Green ch. 5 p. i[21]). This means that there is little difference between the steady-state and unsteady results. Therefore, a steady computation of the rotor blade should produce good pressure distribution predictions.

Haldeman et al. [22, p. 3] stated that an increase in overall pressure levels would be one way of improving the accuracy of the experiment on turbine blade heat transfer. In his experiment, the total pressure ratio was 3.672. The total pressure ratio in this computation is greater, being 4.47.

2.3 Looking at heat transfer

Heat transfer is one of the most important design consideration for the turbine. The efficiency of aircraft engines are heavily dependent upon the turbine inlet temperature. A high inlet temperature results in a high engine performance efficiency. So, there has been a great deal of effort put into pushing the turbine inlet temperature as close to the fuel stoichiometric temperature as possible (Haldeman and Dunn [25]). Due to limitation imposed by the material properties, it becomes very difficult to push the inlet temperature higher, so improved materials which can withstand higher temperatures have been sought after. Also, numerous cooling schemes have been another avenue for engineers to implement into turbine blades to increase engine efficiency.

Heat transfer information on turbine blades have not been widely distributed and the effects of turbulence have not been resolved on turbine blades (Galassi, et al.[20]). When analyzing turbine rotors, two of the most influential aspects of the flow are the tip leakage flow and the vortex that it creates. Tallman et al. list six ways [34] that these two flows are detrimental:

- downstream unsteadiness as seen by a relatively moving nozzle row
- obstruction of primary flow through rotor passage
- production of aero-thermal losses and entropy within rotor
- reduction of blade loading near tip
- adds three-dimensionality to flow-field
- transport of high-temperature fluid toward the airfoil

Ameri et al. [1] found two dominant vortical structures in the recessed tip which strongly affected the heat transfer rate on the surface of the blade tip. They also discovered that the areas where the vorticies exited the recessed region were the same areas that high heat transfer rates occurred. Since the heat transfer on the vane and blade surfaces will be the focus of this paper, the isothermal boundary condition must be applied to all physical boundaries in order to compute the heat flux on the blade surfaces and endwalls. Ameri et al. [9] also found that there was some difference in the time-averaged blade surface heat transfer and the steady blade surface heat transfer.

The computations will be steady-state meaning that the flow parameters do not change with respect to time after convergence has been reached. Previous computations have shown that the effect of wake passing from an upstream wake of a vane has little effect on the heat transfer for the blade tip. However, the effect of wake passing on the blade surface is significant on the suction side of the blade.

2.4 Stator/Rotor Interaction:

In a steady simulation the two blade rows are run in separate simulations. In reality, the flow from the vane will have interaction effects on the flow through the rotor blade. There are thermal wakes and momentum wakes behind the vanes. Unfortunately, the steady rotor blade simulation will not accurately capture these effects. Other interaction effects between the stator and rotor include pressure waves and shock waves near the interface of the exit of the stator and the inlet of the rotor.

There are three flow parameters that need to be calculated from the exit of the stator vane for the inlet boundary conditions of the rotor blade. They are total pressure

distribution, total temperature distribution, and the velocity component angles at the interface. The velocity component will be used to calculate the tangential and radial angles. The total pressure and total temperature distribution must also be calculated at the exit of the stator case to be used as inlet boundary conditions for the rotor blade case. See Section 7.1.3 for details.

It was found that a steady cascade analysis of the blade, which does not include the effect of rotation, develops erroneous heat transfer results. Spinning the rotor blade at design conditions are critical to obtaining accurate heat transfer results on the surface of the blade (Ameri, et al. [9]). Ameri et al. [10] found that there was no significant difference between the unsteady mean and steady heat transfer on the tip. Hence, performing a steady computation on the rotor tip heat transfer should produce good results.

2.5 Flow Solver Details:

This thesis uses TURBO. Tallman et al. [34] has done a very similar project by comparing CFD results to the experimental data by Haldeman [24] using Tacoma, a General Electric Company CFD flow solver. Both flow solvers, MSU-TURBO and Tacoma, are 3-D, compressible, Reynolds-averaged Navier-Stokes CFD solvers. Tallman used a k-ω turbulence model. The turbulence model used in this thesis was the low reynolds number form of the CMOTT $\kappa - \varepsilon$ model (Shih, et al. [31]). It is a two-equation model of transportation of turbulent kinetic energy and dissipation rate. Some numerical scheme features include:

- N-S equation with $\kappa - \varepsilon$ turbulence model in rotating frame

- Finite volume discretization
- High-order fluxes based on Roe scheme
- Newton and Gauss-Seidel Relaxation

The $\kappa - \varepsilon$ turbulence model incorporates the use of damping functions to improve near wall predictions. See appendix for more details. This computer code has been implemented to run on multiple processors and uses MPI (Message Passing Interface) for parallel processing. The simulation will be run on the Ohio Supercomputing Center parallel processors for faster results.

CHAPTER 3

GRID GENERATION

The first step in conducting computation fluid dynamics simulations is generating an appropriate grid for the problem. There are a number of steps required in order to generate a grid that is suitable for the given problem. The steps taken to generate the grids used in this simulation will be discussed in detail for the benefit of others and for future validation purposes.

3.1 Grid Generation method

The generation of a good grid is essential for an accurate CFD run. The quality of a grid is critical for maintaining accuracy and dictates the efficiency of a Navier-Stokes flow solution (Chandi and Lee [14]). There were several requirements that had to be met in order for the grid to be useful for the computer simulation. The requirements included the grid having to be structured and clustered at all physical surfaces. GridPro, an automatic multiblock grid generator was used to generate the grids used in this

simulation. GirdPro produces grids with structured, smooth, and orthogonal elements throughout the volumetric region. This is made possible through the use of highly advanced mathematical algorithms.

3.1.1 Grid

A grid, or a mesh, is defined as a computational domain. The grid is made up of an array of cells that fill a three dimensional region of space.

3.1.2 Clustering

Clustering is a very important component of the grid. The clustering command increases the grid density near a surface. An increase in grid density is desired for all physical boundaries. This is especially important for viscous flow simulations. Clustering of the grid in this case is done on the hub, casing, and vane and blade surfaces. The stator topology is displayed in Figure 3.1.

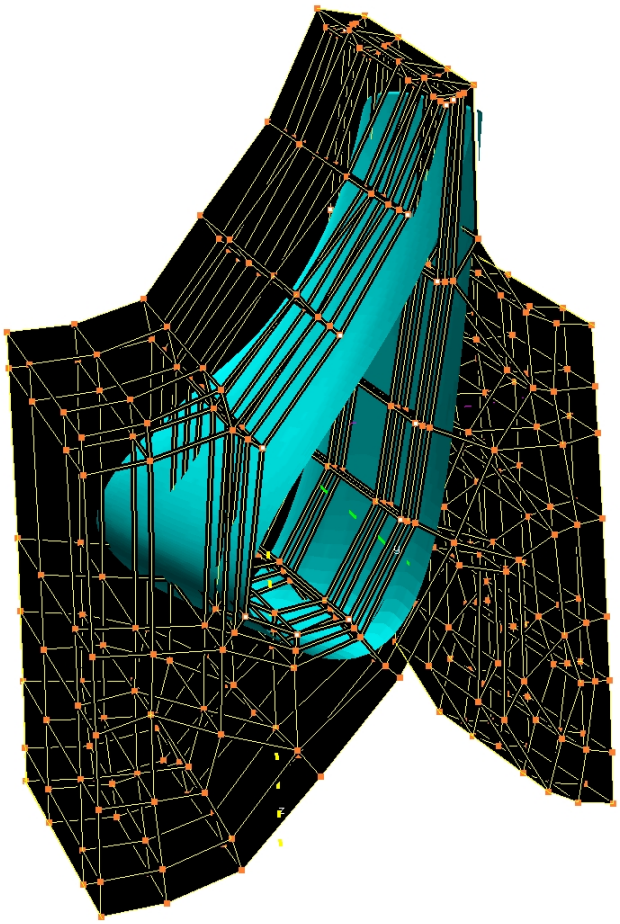

Figure 3.1: Stator Grid Topology

The topology gives the mathematical algorithm in GridPro guidance in determining the grid that will be produced. In GridPro, the surfaces must be assigned to their appropriate topology points in order to generate a suitable mesh that accurately defines the region intended. GridPro will use the surface assignments to produce a grid that fulfills the restrictions imposed upon the topology. Also, GridPro allows a user to assign the boundary conditions on each surface. On the stator grid, the following boundary conditions were specified: periodic boundary conditions, inlet, exit, isother-

mal hub, isothermal casing, and isothermal vane surface. The density of the grid could be set by the user as well. A user can specify a fine grid or a coarse grid depending on what the user needs. Then, the grid was ready to be produced, so the griding process began and it kept iterating and converging until all of the folds in the grid were taken out. A fold in a grid is defined as a situation where the regions of two cells overlap each other. This is also known as a cell with a negative volume. A detailed description of clustering commands are listed in the appendix.

The rotor topology is displayed in Figure 3.2.

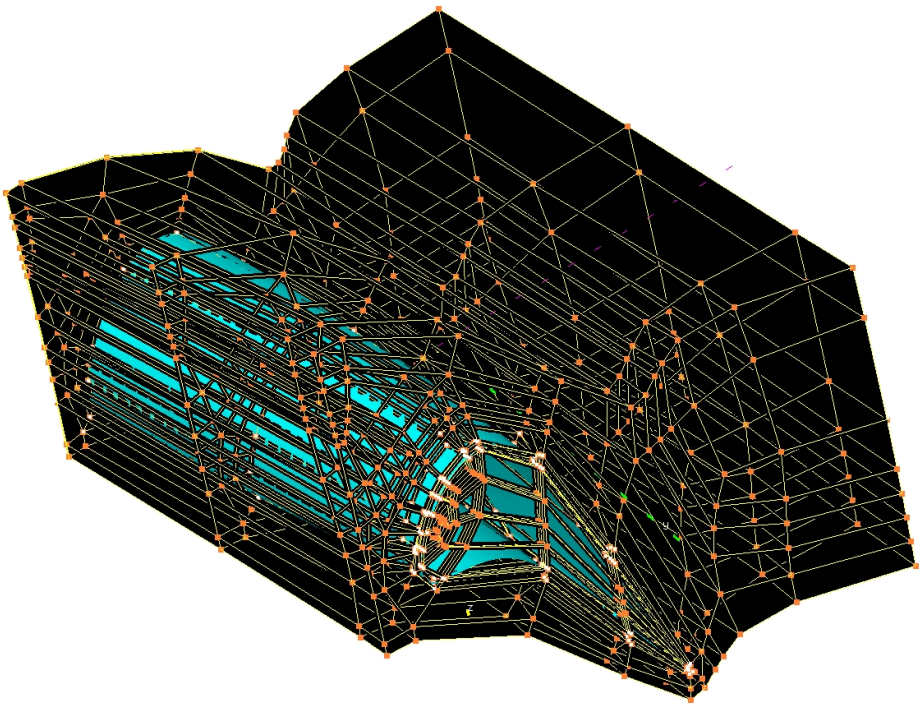

Figure 3.2: Rotor Grid Topology

3.1.3 Quality Check

Running the quality check function is also another condition that must be passed before moving on from each step. The quality check function can be started by clicking on the quality check button on the lower right hand menu when the user is under the grid viewer mode. The quality check function provides a status report on block count, cell count, fold count, skewness, warpage, stretching ratio, smoothness, and aspect ratio. The most important condition that must be met is the condition that there would be zero folds in the grid. The CFD code will not be able to run if there are any folds in the grid.

The total cell count for both vane and blade grids is 2,461,740. This is a relatively fine grid. This cell count is also significantly higher than the number of cells used in a CFD case on heat flux by Haldeman et al. [22]. They used a total of 730,000 cells. Their conclusion was that the results indicated a need for changes in grid refinement. The significantly higher cell count in this experiment should give more accurate results.

3.2 Merging

Merge is a GridPro command that allows a user to combine several smaller elementary blocks into what GridPro calls a superblock. Basically, the merge command combines several small blocks into fewer big blocks. However, there are limitations as to how the blocks can be merged and how many can be merged. This is dependent on how the block grids are assembled and put together. See the appendix for details.

3.3 Y+ Calculator

The value y+ is a non-dimensional wall distance for flows that are bounded by walls. Inspecting the y+ value is important because the value needs to be between 0 and 2 for the first grid point. If the y+ value is too large, then TURBO will have to estimate the velocity profile in the boundary layer. If the y+ value is too small, then the time steps in the computation will also need to be small. The y+ value can be adjusted by changing the normal wall spacing or the grid resolution near a wall. The reference length is 0.0254m (1 inch in S.I. units). The Reynolds number based on a reference length of 0.0254m and a reference velocity of 498.8 m/s is 873,084. The normal spacing specified using GridPro is 1E-5. The present computation has a y+ $\approx$ 0.38 for the 1st grid point off the blade surface and endwalls.

$$y^+ = \frac{u_* y}{\nu}$$

$$\frac{u_* y}{\nu} = \left[\frac{\frac{y}{X_{ref}} \cdot \frac{u_*}{a_0}}{\frac{\nu}{\nu_{ref}}} \right] \cdot Re_{code}$$

where

$$u_* \equiv \sqrt{\frac{\tau_w}{\rho}}$$

and

$$\tau_w = \mu \left(\frac{\partial u}{\partial y} \right)_{y=0}$$

thus,

$$y^+ = \left[\frac{y \cdot \sqrt{\mu \left(\frac{\partial u}{\partial y} \right)_{y=0}} \cdot \sqrt{1/\rho}}{X_{ref} \cdot a_0 \cdot \frac{\nu}{\nu_{ref}}} \right] \cdot Re_{code}$$

CHAPTER 4

INTERFACE MATCHING

An unsteady computation would require that the two blade rows have matching grid lines in the circumferential direction. An unsteady case was planned but was never performed due to time constraints. This procedure could be used in the future for unsteady computations. The grid lines that run in the circumferential direction must be matched. This is done so that the the two grids can be run together in an unsteady CFD case.

4.1 Interface code

There are several steps in the interface matching process. A code is written that will produce temporary blocks to be welded to. GridPro has a 'weld' function that allows two grid blocks with the exact same dimensions to conform to each other. The way that the 'weld' function was used for the purpose of this case was to conform the exit grid block of the stator and the inlet grid block of the rotor to the same interface. Thereby

the exit of the stator and the inlet of the rotor would be matched. The way that a matched interface is defined in this thesis is the condition in which the grid lines that run in the circumferential direction on the patch which represents the stator inlet and the one that represents the rotor inlet match. In other words, all the grid lines running in the periodic direction in both the exit of the stator and the inlet of the rotor are at the same radius away from the center of the turbine. These lines at constant radius from the center of the turbine will be termed radial lines. Another way of saying this is that as the grid point index increases along the radial direction in one block, the other block must have its grid lines at the same radial location at its corresponding grid point index.

The code written for specific purpose of matching the interface is called 'interface.f". First the exit block of the stator grid needs to be separated from the rest of the stator grid. Also, the inlet block of the rotor grid needs to be separated from the rest of the rotor grid. This code will take the exit of the stator and the inlet of the rotor and create temporary grids for these specific grid to match with. Refer to the appendix for the code.

4.2 GridPro: Weld function

The weld function is a useful tool in GridPro in which users can modify up to two grids simultaneously so that the grids match circumferentially. However the limitation of this function is that the two blocks being welded together must be of the same dimensions and must contain the same number of cells. The interface code provides the necessary files for GridPro to match the two blocks correctly. Take the exit block of the

stator and name it exit.p3d and the inlet block of the rotor called inlet.p3d and convert it to GridPro format. Also, take the blocks produced by interface.f, called stator_exit.p3d and rotor_inlet.p3d and convert them to GridPro format as well. Then, the GridPro function called weld is used to conform exit.tmp to stator_exit.tmp(temporary block). Also, inlet.tmp is conformed to rotor_inlet.tmp.

The hub surface is on the bottom and casing surface is on top. One can easily see that the circumferential lines do not match up perfectly at the interface(Figure 4.1). After the exit of the stator and the inlet of the rotor are run through the welding function, the grid lines running in the circumferential direction match at the interface (Figure 4.2).

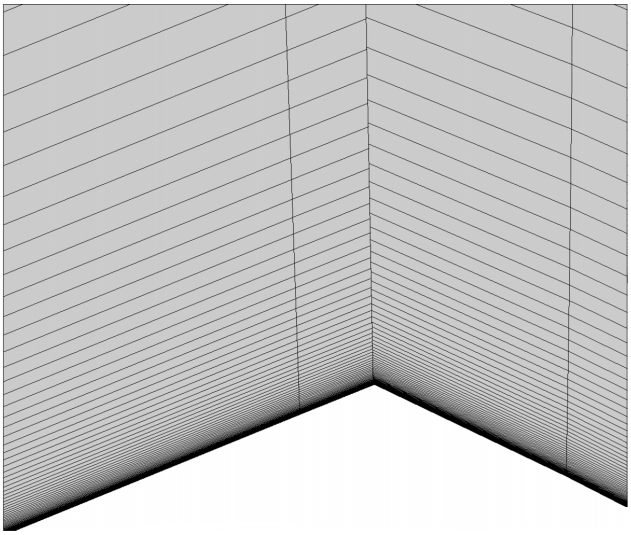

Figure 4.1: Original Stator-Rotor Interface (hub region) (stator on the left, rotor on the right)

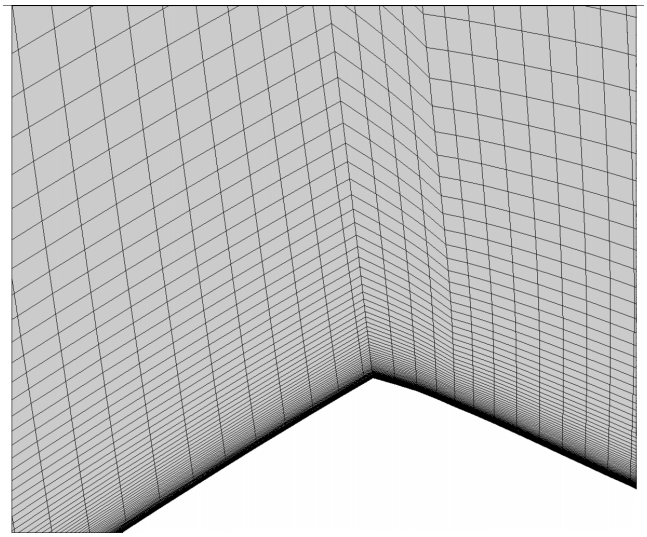

Figure 4.2: Matched Stator-Rotor Interface;

The final product is a stator and rotor that are both clustered, merged into superblocks, and are also matched at the interface. The result is displayed in Figure 4.3.

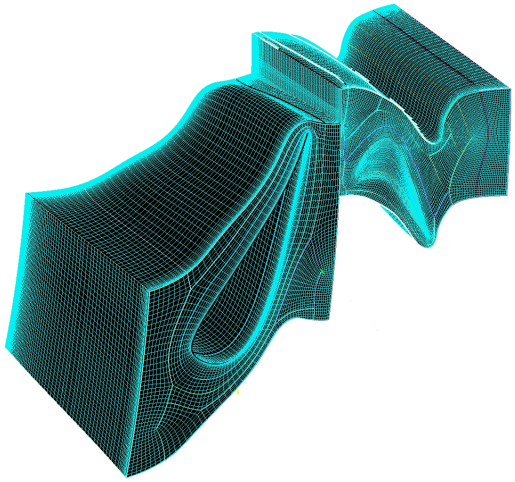

Figure 4.3: Stator and rotor grid clustered and matched at the interface

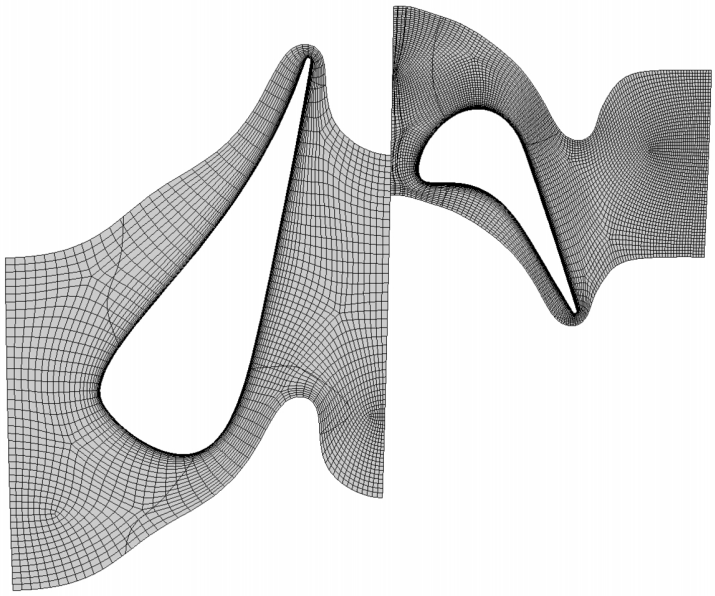

Figure 4.4: Cross-section of H-O 2-blade-row grid

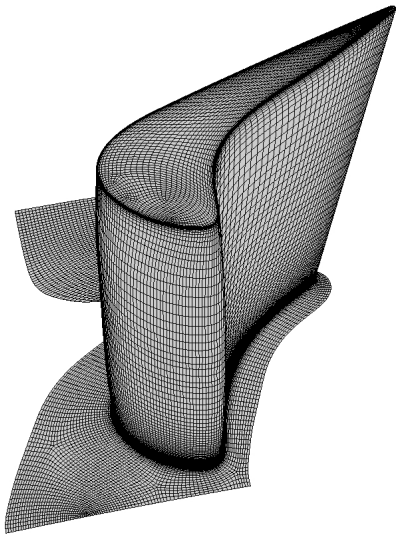

Figure 4.5: Rotor Blade Mesh

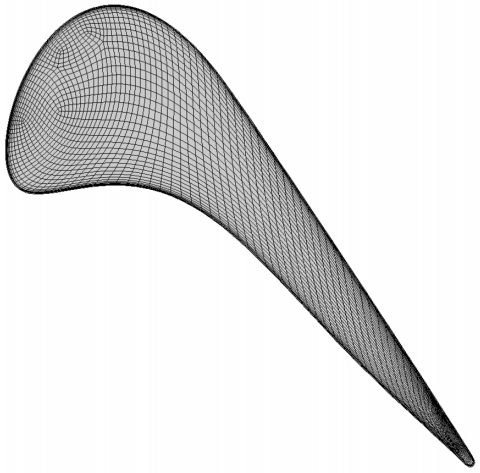

Figure 4.6: Rotor Tip Mesh

4.3 Details of the final grid structures

The stator vane contains 156 cells in the span-wise direction throughout the entire grid. The vane-to-vane direction contains 73 cells. There are 58 cells on the pressure side of the vane surface and 51 cells on the suction side of the vane surface in the axial direction. The rotor blade contains 122 cells in the span-wise direction and 161 cells along the blade surface axially. The section between blades contain 101 cells in the blade-to-blade (periodic) direction. The stator grid contains a total of 709,900 cells and the rotor grid contains a total of 1,751,840 cells. The entire grid (stator and rotor grids) has a combined total of 31 blocks. The cell count is 2,461,740. There are 156 nodes from the hub to the tip. There are 36 nodes across the tip gap in the radial direction. The grid has zero folds. The grid is very fine near the vane and blade surfaces and near the hub, casing, and rotor tip surfaces.

CHAPTER 5

HEAT CONVECTION

This paper is focused on the heat transfer on the surface of a rotor blade. There are three basic modes of heat transfer: conduction, convection, and radiation. This paper will focus on the heat transfer mode of convection. There are two modes of heat convection, free convection and forced convection. The mode of heat convection in this thesis is forced convection because the flow field is created by forces outside of the thermal process. Heat convection occurs when heat energy is transferred between a moving fluid and a surface at different temperatures. The kinetic energy of the fluid is converted to internal energy as it is slowed down next to the surface. The speed of the particles on the surface is zero relative to the body. Heat transfer occurs in this thin layer of molecules next to the surface. Heat is then conducted into the surface from the higher temperature air. The result is that the surface of the material increases in temperature and the fluid loses energy. Heat convections ensures that other parts of the material replenish energy to the gasses that have cooled so that the process of heat transfer can continue.

5.1 Heat Convection Equation

The heat convection equation will be used to analyze the heat flux which will then be used to calculate the heat transfer coefficient. The heat convection on the surface of the rotor blade is calculated numerically. The heat convection on the blade is represented by the variable, q_{wall}. This constant of proportionality is usually dependent upon temperature. The temperature of the wall will be determined by input parameters and will be a constant, so the thermal conductivity term will also be a constant.

$$q = -k\frac{\partial T}{\partial x}$$

also, $q = h\Delta T$ (convective heat flux).

so, at the interface of a wall,

$$k\frac{dT}{dx} = h\Delta T$$

5.2 Normalizing the heat flux term

It is necessary to normalize the heat flux term in order to relate heat flux to temperature gradient. The TURBO code calculates the heat flux terms in non-dimensional values so there is a need for a formula for the heat flux in terms of non-dimensional values.

$$q_{wall} = -k_{wall}\frac{d\overline{T}}{d\overline{n}}\,|_{turbo}\cdot\frac{T_0}{x_0}$$

$$q_{wall} = \frac{-c_p\mu_{wall}}{Pr}\cdot\frac{T_0}{x_0}\frac{d\overline{T}}{d\overline{n}}\,|_{turbo}$$

$$q_{wall} = \frac{-\gamma \cdot R \cdot T_0}{(\gamma - 1) \cdot Pr \cdot x_0} \cdot \frac{d\overline{T}}{d\overline{n}} \mid_{turbo} \cdot \overline{\mu}_{wall} \cdot \mu_0$$

$$q_{wall} = \frac{-\rho_0 \cdot a_0^3}{Pr \cdot (\gamma - 1)} \cdot \overline{\mu}_{wall} \cdot \frac{d\overline{T}}{d\overline{n}} \mid_{turbo} \cdot \frac{\mu_0}{\rho_0 \cdot x_0 \cdot a_0}$$

$$q_{wall} = \frac{-\rho_0 \cdot a_0^3}{Re_0 \cdot Pr \cdot (\gamma - 1)} \cdot \overline{\mu}_{wall} \cdot \frac{d\overline{T}}{d\overline{n}} \mid_{turbo}$$

note:

$$\frac{d\overline{T}}{d\overline{n}} \mid_{turbo} = \frac{d\overline{T}}{d\overline{n}} \mid_{f.v.} \cdot \gamma_0$$

so,

$$q_{wall} = \frac{-\rho_0 \cdot a_0^3}{Re_0 \cdot Pr \cdot (\gamma - 1)} \cdot \overline{\mu}_{wall} \cdot \frac{d\overline{T}}{d\overline{n}} \mid_{f.v.} \cdot \gamma_0$$

also,

$$\overline{\mu}_{wall} = \bar{T}^{2/3}$$

thus:

$$q_{wall} = \frac{-\rho_0 \cdot a_0^3}{Re_0 \cdot Pr \cdot (\gamma - 1)} \cdot \left(\bar{T}^{2/3}\right) \cdot \frac{d\overline{T}}{d\overline{n}} \mid_{f.v.} \cdot \gamma_0$$

5.3 Heat Transfer Coefficient

$$h = \frac{q_{wall}}{T_{wall} - T_{ref}}$$

In this computation, the following condition is set:$T_{wall} = 0.7 \cdot T_{ref}$. An isothermal boundary condition was imposed upon the blade surface because heat transfer was the

focus of this thesis.

The wall temperature of the blade is set to be at 0.7 times the reference temperature. The metal temperature in the experiment was 2100R (1166.6 K) which is close to the thermal limit of the material. The free-stream temperature in the experiment is 3000R (1666.6 K) which means that $T_{wall} = 0.7 \cdot T_{ref}$. The reference temperature for the computation was set to only 627K which is significantly less than the experimental temperature. However, since the all the heat transfer results are non-dimensionalized, this should not be a concern.

This equation is also normally referred to as Newton's Law of Cooling which takes the form of

$$q_{wall} = h \cdot \left(T_{wall} - T_{ref}\right)$$

Heat transfer coefficient can be thought of as the inverse of thermal resistance. This coefficient can be used to obtain an expression for Nusselt number which is a non-dimensional value that is usually used for looking at heat transfer.

5.4 Stanton Number

The Stanton number is another dimensionless number which relates the heat transferred into a fluid to the thermal capacity of the fluid. The Stanton number is the preferred and appropriate method of making comparisons of computational data with the experimental data. Both computational and experimental sets of data need to be non-dimensionalized in order to be properly compared. The following is a definition of the Stanton number in terms of convective heat transfer coefficient, density of the fluid, specific heat of the fluid, and the velocity of the fluid.

$$St = \frac{h}{c_p \cdot \rho \cdot V}$$

since $h = \frac{q_{wall}}{T_{wall} - T_{ref}}$, and knowing $\dot{m} = \rho \cdot A \cdot V$, the expression for Stanton number can be rewritten as:

$$St = \frac{q_{wall}}{\left(\frac{\dot{m}}{A}\right) \cdot c_P \cdot \left[T_{wall} - T_{ref}\right]}$$

and then more simply,

$$St = \frac{q_{wall}}{\left(\frac{\dot{m}}{A}\right) \left[\left(c_P \cdot T\right)_{wall} - \left(c_P \cdot T\right)_{ref}\right]}$$

$$St = \frac{1}{\rho \cdot V \cdot C_P} \cdot \frac{-k \cdot \frac{dT}{dn}}{T_{wall} - T_{ref}}$$

knowing:

$$Pr = \frac{\mu_{wall} \cdot C_P}{k}$$

rearranging:

$$\mu_{wall} = \frac{Pr \cdot k}{C_P}$$

$$\mu_{wall} = \rho_{wall} \cdot \nu_{wall}$$

multiply and divide by μ_{wall} and simplify to obtain:

$$St = \frac{-\frac{dT}{dn}\big|_{wall}}{T_{wall} - T_{ref}} \cdot \frac{\mu_{wall}}{\rho \cdot V} \cdot \frac{1}{Pr}$$

An expression in nondimensional terms:

$$St = -\left[\frac{\frac{d\bar{T}}{dn}|_{wall}}{\bar{T}_{wall} - \bar{T}_{ref}}\right] \cdot \left[\frac{\bar{\mu}_{wall}}{\bar{\rho} \cdot \bar{V}}\right] \cdot \left[\frac{1}{Pr}\right] \cdot \left[\frac{\mu_{ref}}{\rho_{ref} x_{ref} a_0}\right]$$

more simply:

$$St = -\left[\frac{\frac{d\bar{T}}{dn}|_{wall}}{\bar{T}_{wall} - \bar{T}_{ref}}\right] \cdot \left[\frac{\bar{\mu}_{wall}}{\bar{\rho} \cdot \bar{V}}\right] \cdot \left[\frac{1}{Pr}\right] \cdot \left[\frac{1}{Re_{ref}}\right]$$

CHAPTER 6

PREPROCESSOR

Preprocessor is a fortran code, written by Vikram Shyam, which takes files produced by GridPro and creates files that TURBO requires for the code to run properly. See the appendix for details.

The code ran with the $\kappa - \varepsilon$ turbulence model at a Reynolds number of 876,774 for 40,000 iterations. For a list of input parameters, see the appendix.

6.1 Block orientation

Each grid is usually made up of several blocks. In this case, the stator vane is made up of 11 individual blocks and the rotor is made up of 20 blocks resulting in 31 total blocks. Gumbo, or Graphical Unstructured Multiblock Omnitool for Structured Grids, is a tool used for working with grids. Each block must have indicies that obey the right-hand orientation. TURBO requires certain rules for block orientation. These rules are in the appendix.

CHAPTER 7

TURBO

There are several things to consider before running TURBO code. This section will discuss some of the more important input parameters. For the steady case, the stator and rotor blade rows are run separately. First, the stator vane case is run until convergence and then the exit profile is used as the inlet profile for the rotor blade case. Turbulence_model must be set to 5 in order for TURBO to use the $\kappa - \varepsilon$ turbulence model. This case is run with laminar flow conditions until convergence. Once convergence is reached, the case is changed to a turbulent case. The case is run until convergence, and the same process is repeated while lowering the back pressure until the exit pressure profile boundary condition is reached. The exit static pressure on the stator vane case varies around 150kPa. The exit static pressure on the rotor blade case varies around 70kPa.

7.1 Solving for inlet conditions of second blade row

After the steady case for the isolated stator has a converged solution, the steady case for the simulation of the rotor must be carefully set up. There are three essential parameters to be taken from the steady simulation of the stator vane in order for the entire simulation to be accurate. The following are the three critical parameters.

1. Exit profile of the total pressure at the exit of the stator vane
2. Exit profile of the total temperature at the exit of the stator vane
3. Exit profile of the radial and tangential angles of the component velocity vectors at the exit of the stator vane.

7.1.1 Total pressure profile

The total pressure profile can be easily obtained through the FieldView application. The non-dimensional static pressure profile can then be obtained by taking a sliver of the pressure profile and integrating by sweeping the surface from hub to casing surface. This information can be saved in a data file. The values from fieldview must then be multiplied by gamma and the reference pressure in order to get the dimensionalized values since Fieldview's value of pressure is: $P_{FV} = \frac{P_{static}}{P_{ref}}$. Thus, $P_{Total} = P_{FV} \cdot \gamma \cdot P_{ref}$. This should give an accurate total pressure profile along the span of the blades at the interface of the two blade rows.

7.1.2 Total Temperature profile

The total temperature profile can be easily obtained through the FieldView application. The non-dimensional static temperature profile can then be obtained by taking a sliver of the temperature profile and integrating by sweeping the surface from hub to casing surface. This information can be saved in a data file. These values must then be multiplied by gamma and the reference temperature in order to get the dimensionalized values since Fieldview's value of pressure is: $T_{FV} = \frac{T_{static}}{T_{ref}}$. Thus, $T_{Total} = T_{FV} \cdot \gamma \cdot T_{ref}$. This should give an accurate total temperature profile along the span of the blades at the interface of the two blade rows.

7.1.3 Tangential and Radial angles

The simulation produces velocity components in Cartesian coordinates. The tangential and radial angles of the velocity can be related through velocity components in polar coordinates.

$v_r = v \cdot \cos(\theta) + w \cdot \sin(\theta)$

$v_\theta = w \cdot \cos(\theta) - v \cdot \sin(\theta)$

where $\theta = \tan^{-1}(\frac{z}{y})$

The angle that the radial component of the flow would have to turn in order for it to be going axially downstream the turbine will be called the radial angle,α. Also, the angle that the tangential component of the flow would have to turn in order for it to be going axially downstream the turbine will be called the tangential angle, β.

$\alpha = \tan^{-1}(\frac{v_\theta}{u})$

$\beta = \tan^{-1}(\frac{v_r}{u})$

These relations can be used to determine the tangential angle and radial angle of the velocity component profiles at the exit of the stator vane. All of these critical parameters will be used in the input00 file to start the steady simulation of the rotor blade. The velocity components and the pertinent angles are displayed in Figure 7.1.

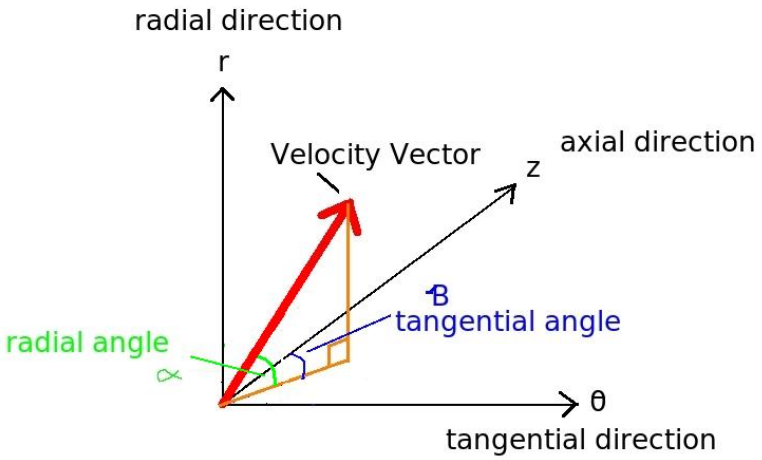

Figure 7.1: Tangential and radial velocities and angles

7.2 Rotation of the rotor blade

The main focus of this thesis is to take a look at the heat transfer on the rotor blade. In this case, the rotor is rotating at 8971 rpm (revolutions per minute). The predictions produced by TURBO will be analyzed and conclusions will be made about the results. Since the velocity vectors in the rotor grid will be in the absolute frame, the velocity vectors will be significantly affected by the rotating blade, and it will be difficult to determine whether the vectors make sense. In order to resolve this issue, the velocity vectors can be viewed in the relative frame. The rotational speed of the blade will

essentially be subtracted and the relative frame will be an easier frame to examine the flow in. The following calculations were performed to calculate the relative frame velocities from an absolute frame.

$$V_{rel} = V_{abs} - \overrightarrow{\Omega} \times \overrightarrow{r}$$

$$V_{rel} = V_{abs} - (\omega_x, \omega_y, \omega_z) \times (0, y, z)$$

since $\omega_y$and $\omega_z = 0$,

$$V_{rel} = V_{abs} - (\omega_x, 0, 0) \times (0, y, z)$$

$$V_{rel} = V_{abs} - (\omega_x, 0, 0) - (0, -\omega_x * z, \omega_x \cdot y)$$

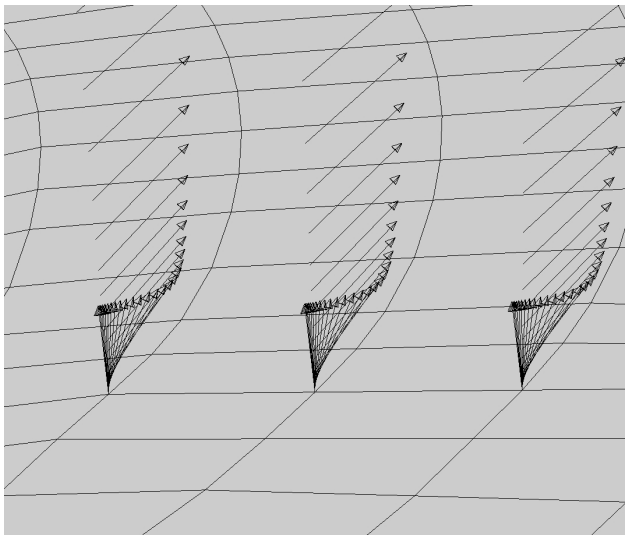

Figure 7.2: Blade Surface Velocity Vectors (Suction Side) in Absolute Frame

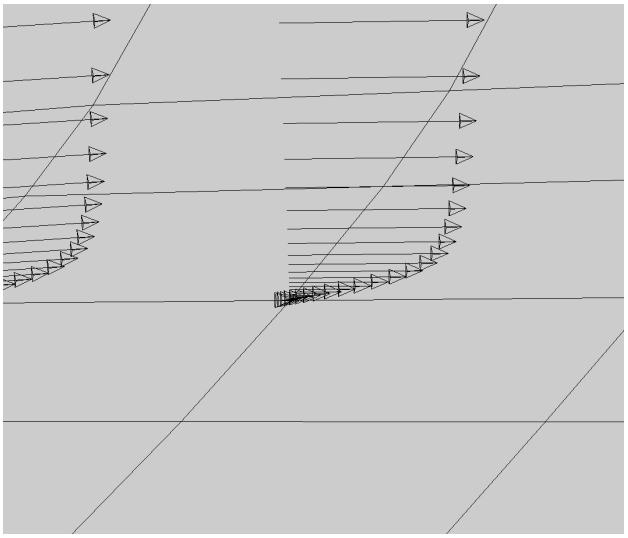

Figure 7.3: Blade Surface Velocity Vectors (Suction Side) in Relative Frame

Notice that the velocities on the blade (Figure 7.2) in the absolute frame are going in the positive tangential direction. This indicates the desired direction of the rotation of the blade. At that exact same point, the velocity vectors on the blade surface in the relative frame are moving along the surface of the blade (Figure 7.3). The rotational wheel speed has been successfully taken out. The velocity vectors at the inlet of the rotor in the relative frame are displayed in Figure 7.3.

The wheel speed of 8971 rpm is chosen for this thesis because the experimental data was gathered from operating at this speed. This thesis will make comparisons with the Re/L = 3.1E6 case. The Reynolds number are very close to the one in the CFD case. The following graph is a comparison of operating conditions between the experiment by Tallman et al. [34] and this thesis.

Parameter	Tallman	Present Computation
Inlet P_0(kPa)	386.8	386.9
Inlet T_0(K)	627.1	627.7
RPM	8970.0	8971.0
Re/L(1/meters)	3.13E6	3.1E6

Figure 7.4: Matrix of Experiments

7.3 BC Profiles

The steady state stator computation was computed using an isentropic inlet. The reference pressure was 386,934 kPa. The reference temperature was 627.711 K. Notice that the static pressure is not constant in the radial direction, instead, it is decreasing as the radius increases. The static temperature profile has a similar trend.

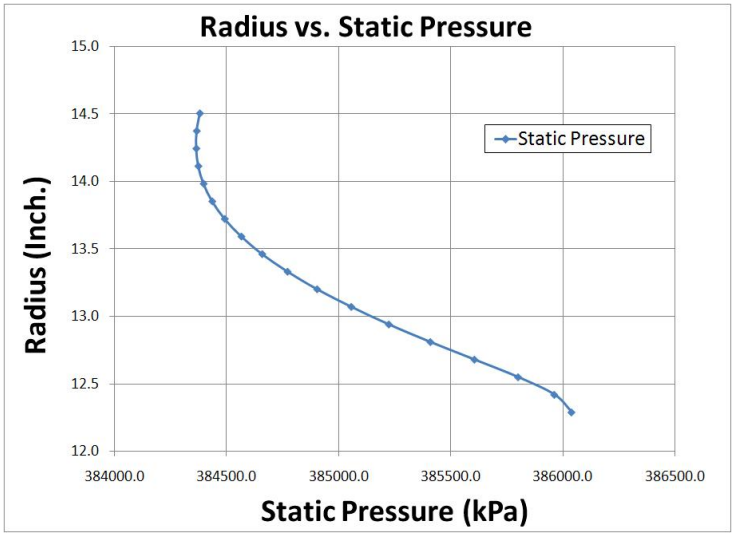

Figure 7.5: Pressure Profile (Stator Inlet)

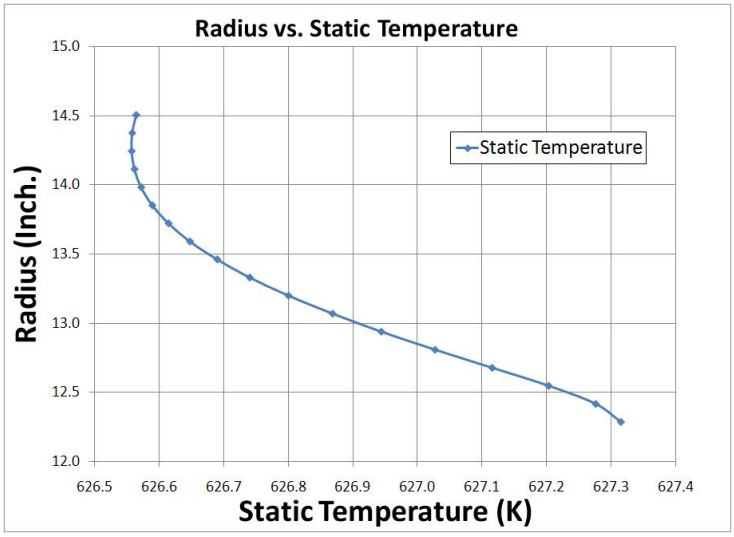

Figure 7.6: Temperature Profile (Stator Inlet)

After the steady stator computation was completed, the static pressure and static temperature profiles were calculated by analyzing the data from a converged solution of the steady stator computation. A static pressure profile was a boundary condition imposed on the exit of the stator vane for the computation. The static pressures input match the computational results. The static temperatures near the hub and casing surfaces are higher because of a phenomenon called the horseshoe vortex and is the result of endwall boundary layer flow stagnating against the airfoil leading edge (Schlichting [29]). See Section 8.3.3 for more details. The following static pressures and static temperatures are normalized by their respective total conditions. The tangential and radial angles were calculated from the x,y,z coordinates and the u,v,w velocities (Section 7.1.3). These pressures, temperatures, and angles are used as the inlet boundary conditions for the steady rotor case.

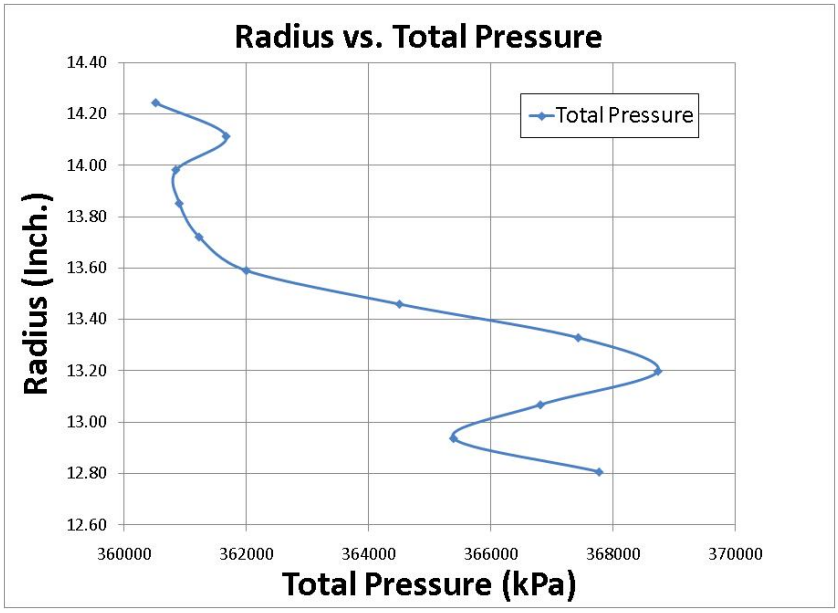

Figure 7.7: Pressure Ratio vs. Radius (Rotor Inlet)

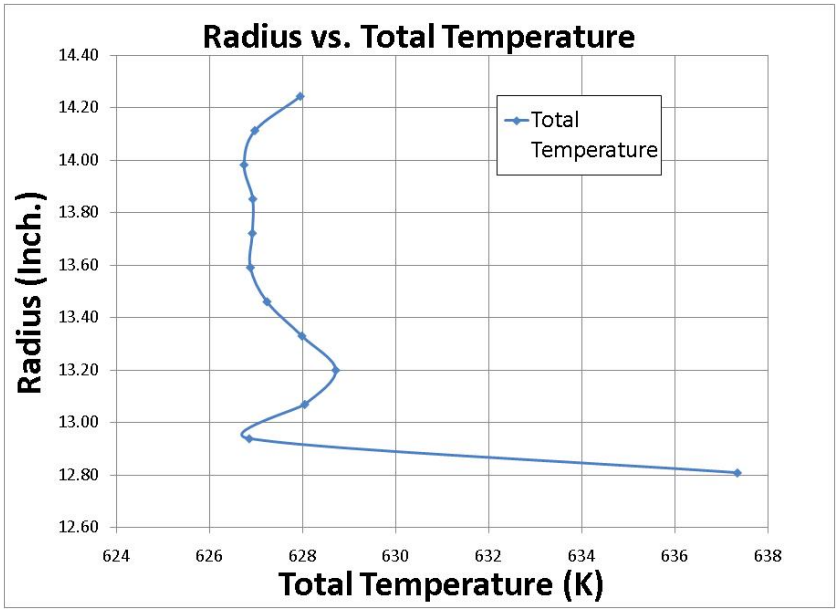

Figure 7.8: Temperature Ratio vs. Radius (Rotor Inlet)

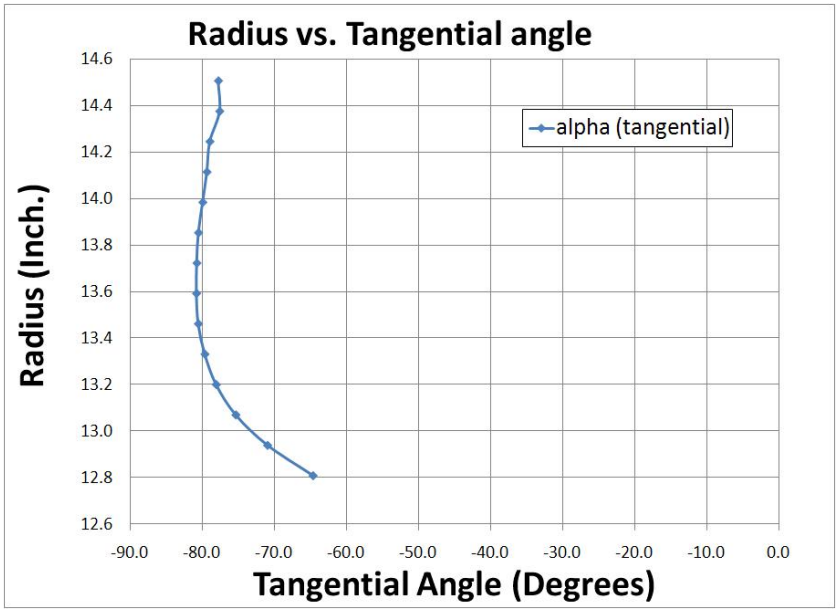

Figure 7.9: Tangential angle vs. Radius (Rotor Inlet)

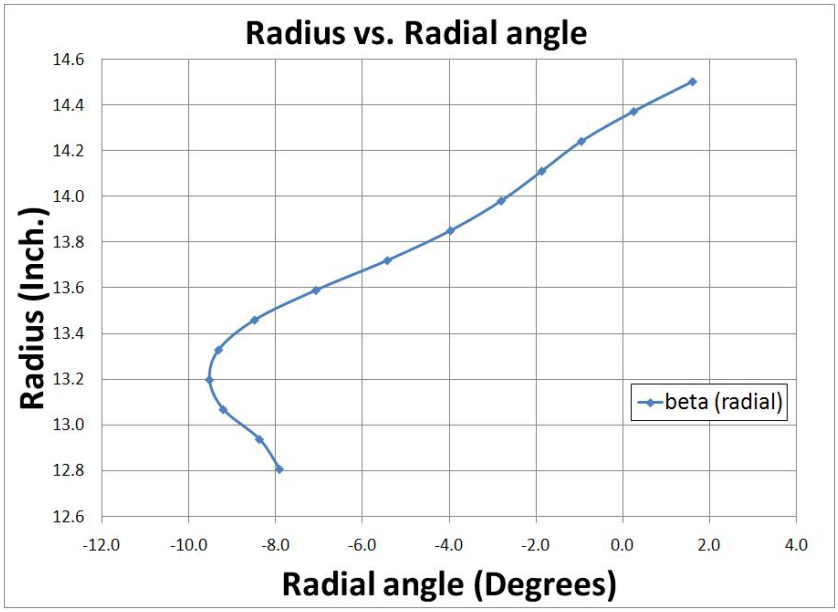

Figure 7.10: Radial angle vs. Radius (Rotor Inlet)

After the steady rotor computation was completed, the pressure, temperature, tangential angle, and radial angle profiles were calculated by analyzing the data from a converged solution of the steady rotor computation. The temperature at the exit of the rotor near the casing surface is higher due to the pressure difference between the pressure and suction surfaces which causes the leakage flow to accelerate and this in turn leads to high thermal loads in the tip gap.

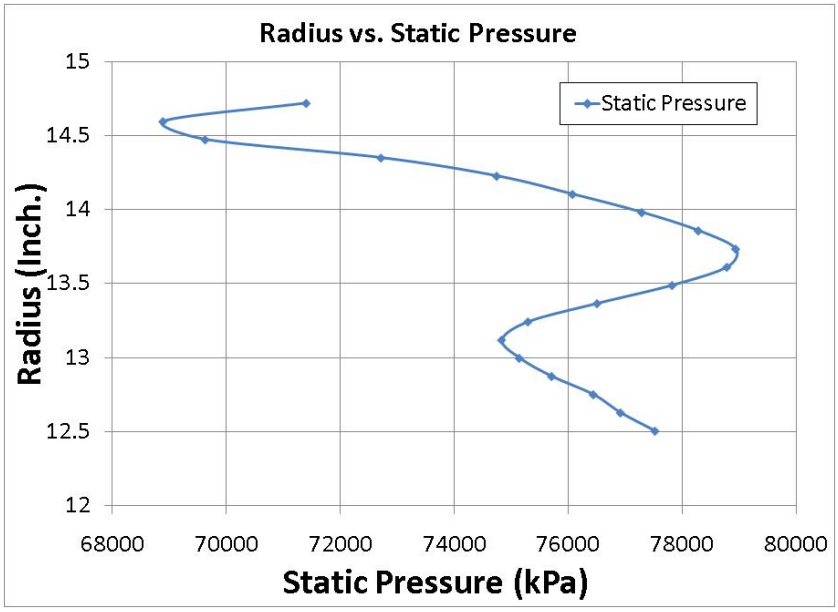

Figure 7.11: Pressure Ratio vs. Radius (Rotor exit)

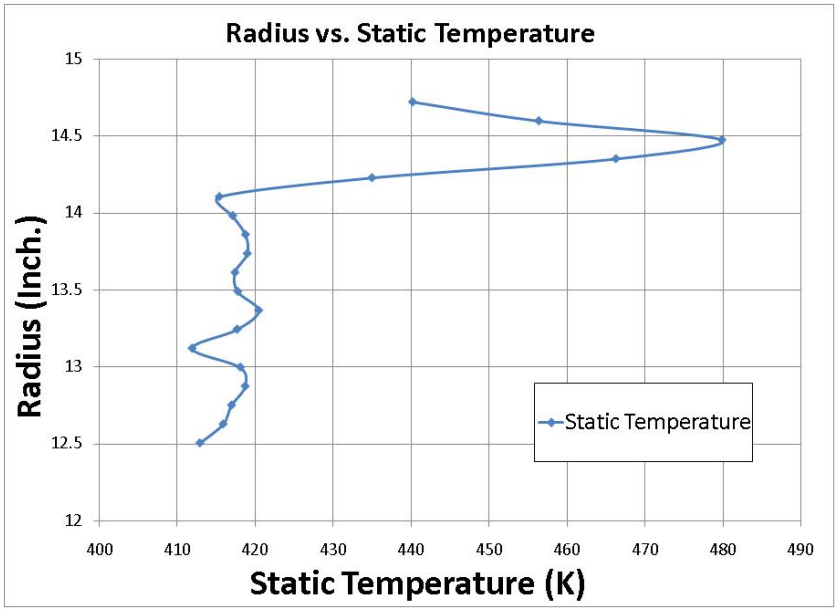

Figure 7.12: Temperature Ratio vs. Radius (Rotor exit)

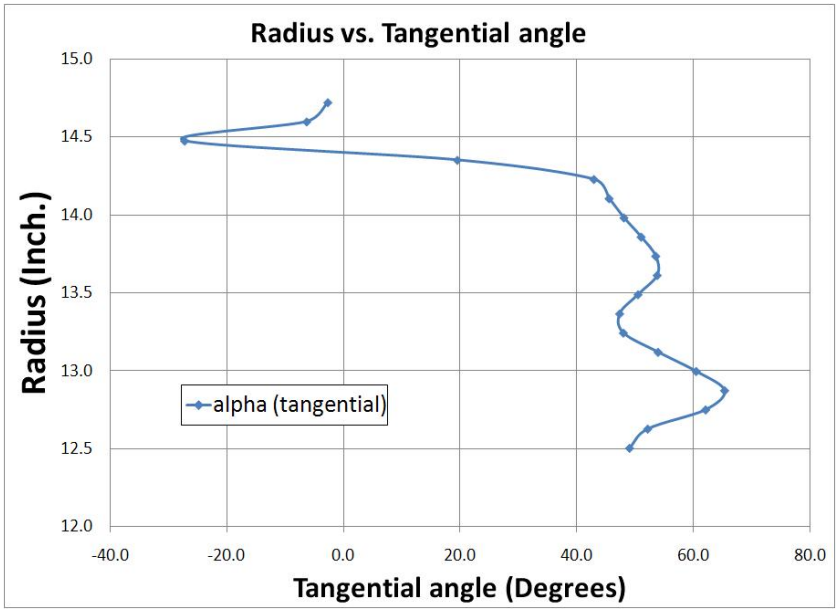

Figure 7.13: Tangential angle vs. Radius (Rotor exit)

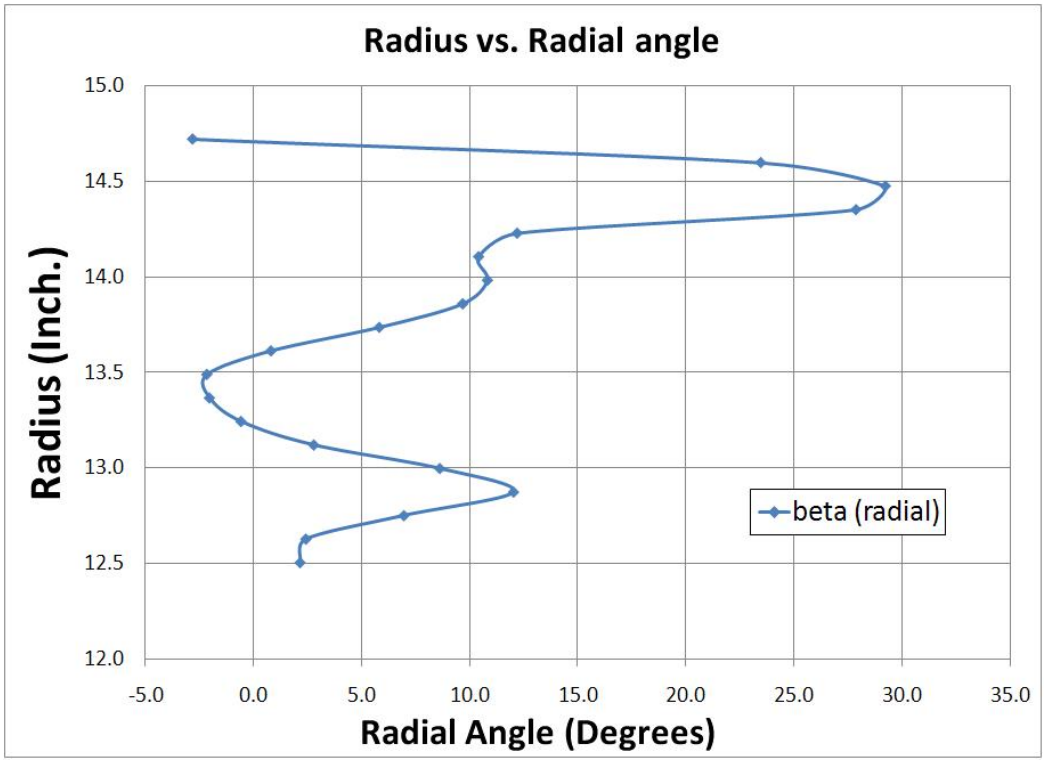

Figure 7.14: Radial angle vs. Radius (Rotor exit)

CHAPTER 8

COMPUTATIONAL RESULTS

8.1 General Remarks

Both computational cases have converged to better than 0.05 percent mass flow error between the inlet and the exit of the respective computational domains. About 40,000 grid iterations were necessary for the convergence of each steady-state case. Convergence of the solution was confirmed by comparing successive iterations of 5000 of the heat transfer results. Also, convergence is evidenced by the smooth contour lines of heat flux displayed in Figure 8.27.

8.2 Vane Computational Results

There is experimental data available for the heat transfer on the surface of the vane for 15%, 50%, and 90% span. These are the locations at which computations were done by Tallman et al. [34]. Comparing the pressure predictions with the measured

pressure distribution is an important first step, because the convective heat transfer in the turbine is a direct result of the complex turbine aerodynamics. If the pressure distributions match, then it is reasonable to draw conclusions about the heat transfer predictions. The experimental measurements for pressure and heat transfer were taken from Haldeman et al. [23].

8.2.1 Vane Surface Pressure Predictions

The x-axis represents the fractional distance away from the leading edge. The negative x values represent the pressure side while the positive x-values represent the suction side. The vane surface location was calculated from the leading edge. The distance between two points axially along the vane surface is given by the following formula with point 1 having coordinates of (x_1, y_1, z_1) and point 2 having coordinates of (x_2, y_2, z_2):

$$S_2 = \sqrt{(x_2 - x_1)^2 + (y_2 - y_1)^2 + (z_2 - z_1)^2} + S_1$$

where S is the curvilinear distance along the vane and blade surfaces in the axial direction.

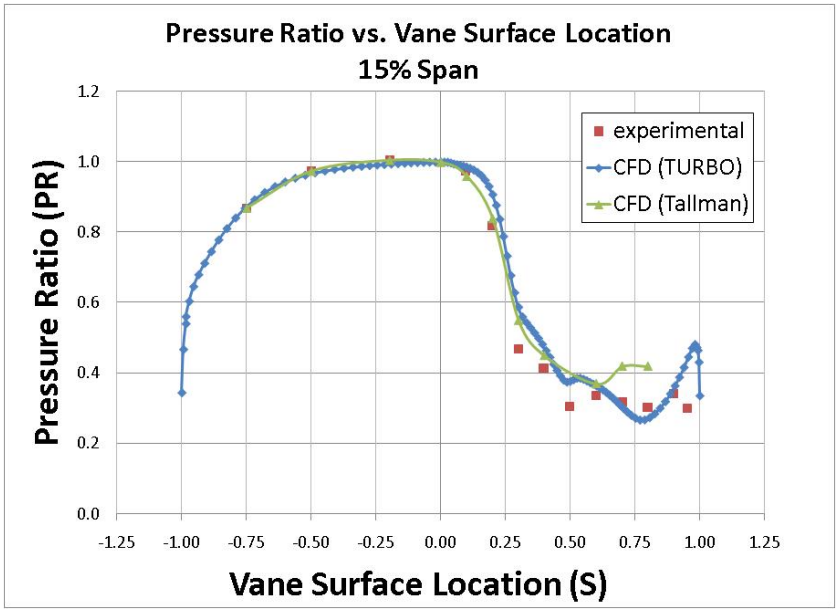

Figure 8.1: Pressure Ratio at 15% Span

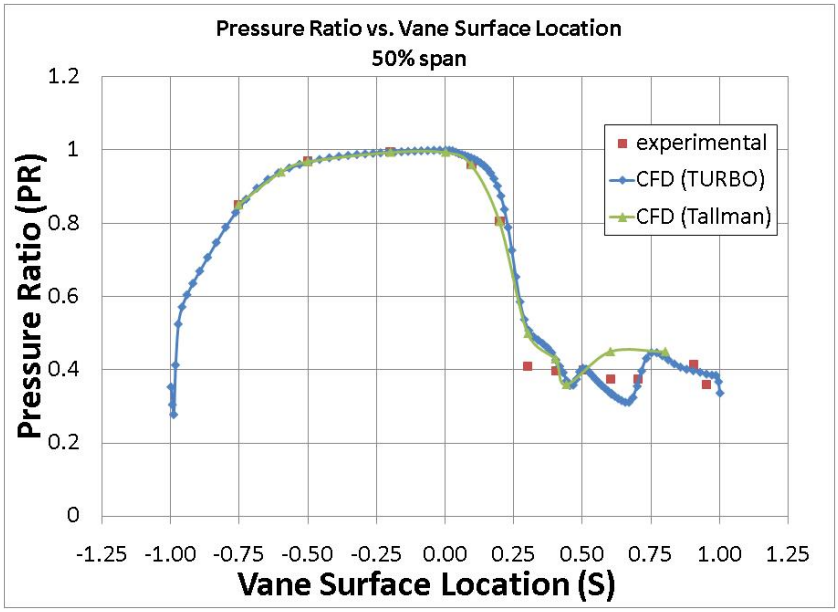

Figure 8.2: Pressure Ratio at 50% Span

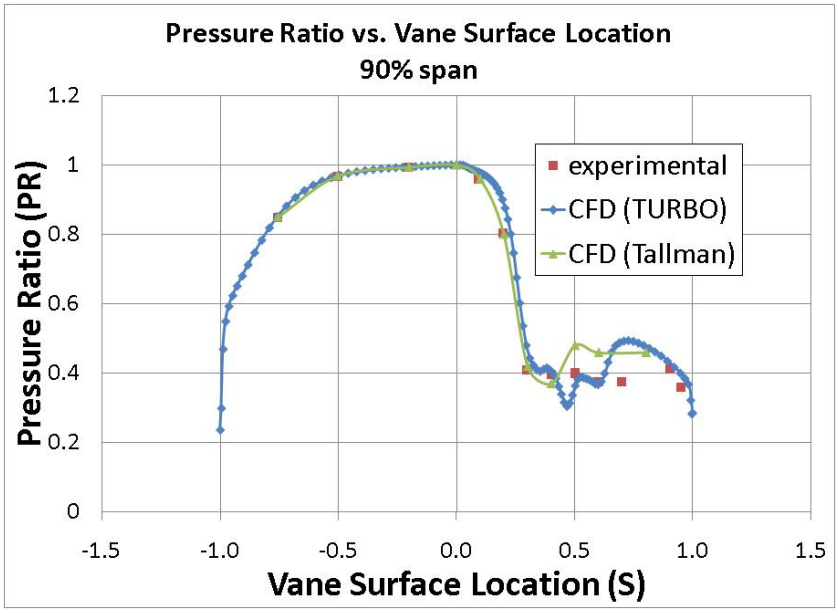

Figure 8.3: Pressure Ratio at 90% Span

The pressure distributions along the surface of the vane match well with the experimental data from Haldeman (Tallman, et al. [34]). The pressure distribution on the pressure side of the vane matches exceptionally well. The pressure distributions are similar on the pressure surface but vary slightly on the suction surface. An area of discrepancy exists between the experimental and computational results in Figure 8.3. The pressure increases in the experimental data at S=0.5 while in the computation, there is a pressure decrease at S=0.5. The pressure increase does increase at a downstream location at S = 0.7.

The experimental results capture pressure waves from rotor blades and other more complex aerodynamics. These predictions are steady-state and there are some aerodynamics that are not captured. However, It was found that the unsteady influence on the vane surface pressure were small (Tallman, et al. [34]). The experimental data

indicates a pressure increase at 90% span at S = 0.4. The steady-state predictions do a good job of capturing this pressure increase.

The Re/L in this simulation is 3.05E6. This is a value very close to one of the Re/L value used by Tallman et al. [34] which was 3.1E6. So, this thesis will compare the data from the Re/L = 3.1E6 case. The Reynolds numbers have a 1.6% difference. Keeping this in mind, we can still draw conclusions about the heat transfer despite the differences. The good fit between computational data and experimental data provides confidence in making conclusions about the heat transfer results. Looking at the pressure distribution is also a good check on the validity of the code.

8.2.2 Vane Surface Heat Transfer

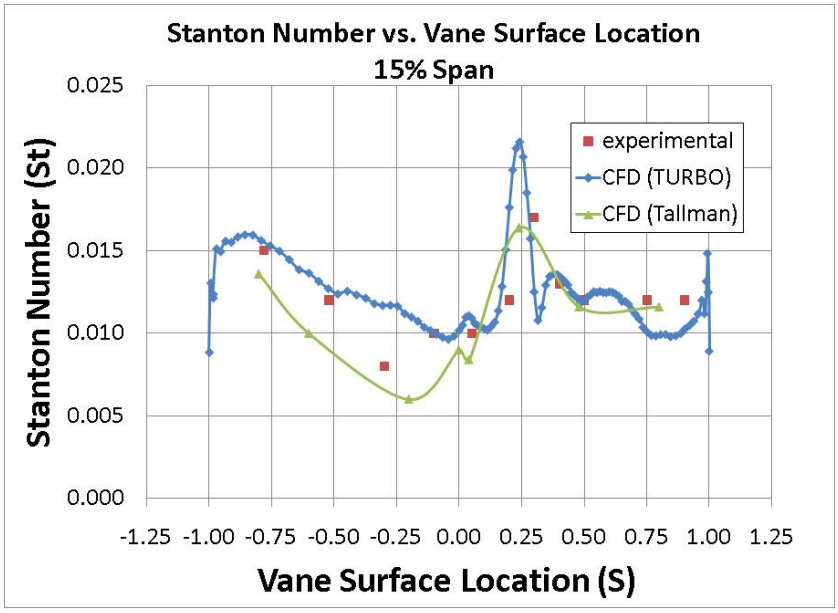

Figure 8.4: Vane Stanton No. 15% Span

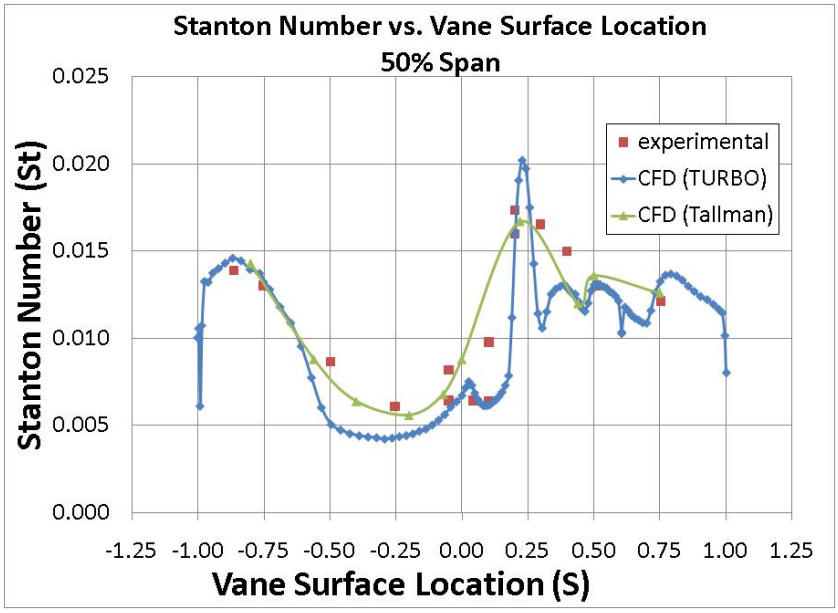

Figure 8.5: Vane Stanton No. at 50% Span

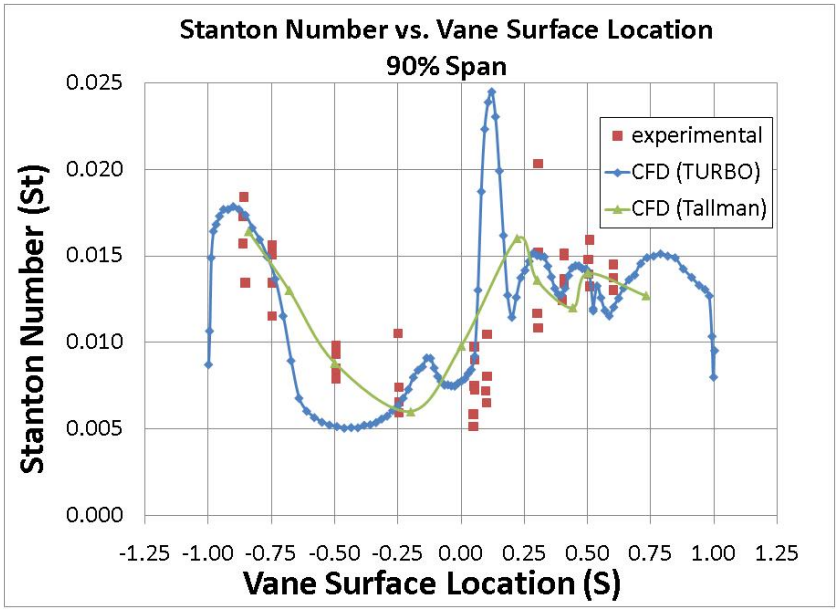

Figure 8.6: Vane Stanton No. at 90% Span

TURBO's computational results fit well with the experimental data. The general trend of the computational data fits well with the experimental results. The computed heat transfer spikes at around S=0.2 at each of the spanwise locations, which matches well with the computations by Tallman et al. [34] and the experimental data by Haldeman [24]. The computational results from TURBO fluctuates a little more than the computation by Tallman et al. [34]. The heat transfer at the trailing edge drops off significantly at all three spanwise locations. This effect is not seen in the computation by Tallman et al. [34].

Peak heat flux occurs in front of the leading edge on the suction surface. The increased heat flux on the leading edge at 90% span may be due to the horseshoe vortex (Figure 8.14).

There are a few places where there is a significant difference between the experimental data and computational predictions. There is a significant difference at 15% span, vane surface location S = -0.4 (pressure side) where the computational results has dramatically over predicted the measurement at that point. One explanation for the difference would be that this area of the vane may be experiencing near-endwall secondary flows. This may also explain the bad fit at 90% span, S = -0.5 (pressure side).

8.3 Blade Computational Results

The rotor blade was run as a separate steady-state case from the steady vane case. The code was run with a spatial accuracy of two. The inlet boundary conditions is radial pressure and temperature profiles along with the tangential and radial flow angles. The

inlet conditions were taken from the converged solution of the steady state vane computation. The exit boundary conditions is a static pressure profile. Consecutive heat transfer predictions at 5000 iterations apart were compared to confirm convergence of the solution.

8.3.1 Blade Surface Pressure Predictions

The pressure distribution of the computation matches up well with the experimental data. The pressure distributions are normalized by the total pressure at the inlet of the stator vane. At S=0.7 of the 15% and 50% span graph (Figure 8.7 and Figure 8.8), there is a sudden increase in pressure from the experimental data. This indicates the existence of the trailing edge of a shock at that point. This effect is seen at 15% span and 50% span. However, it is not seen in the 90% span measurement. The pressure measurements at the 90% span line are influenced by both a shock and the leakage vortex, which would result in less of a dramatic spike in pressure. This effect is captured well by the CFD predictions by Tallman et al. [34]. It is also captured by the TURBO computation.

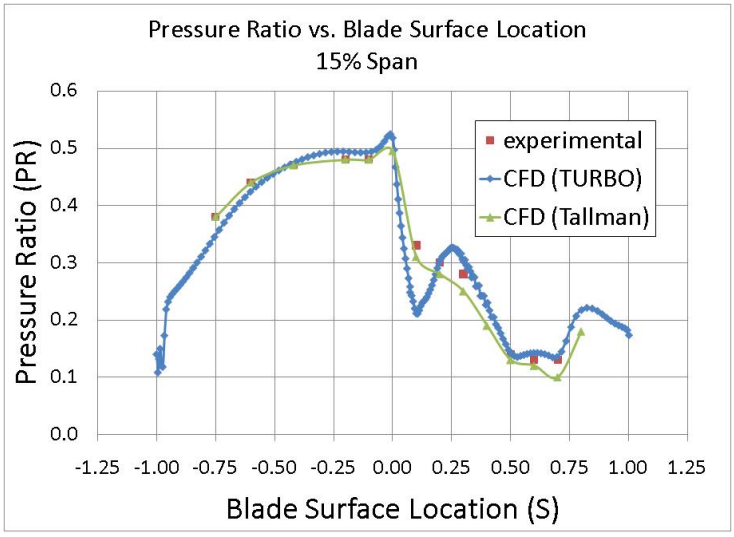

Figure 8.7: Blade Pressure Distribution at 15% span

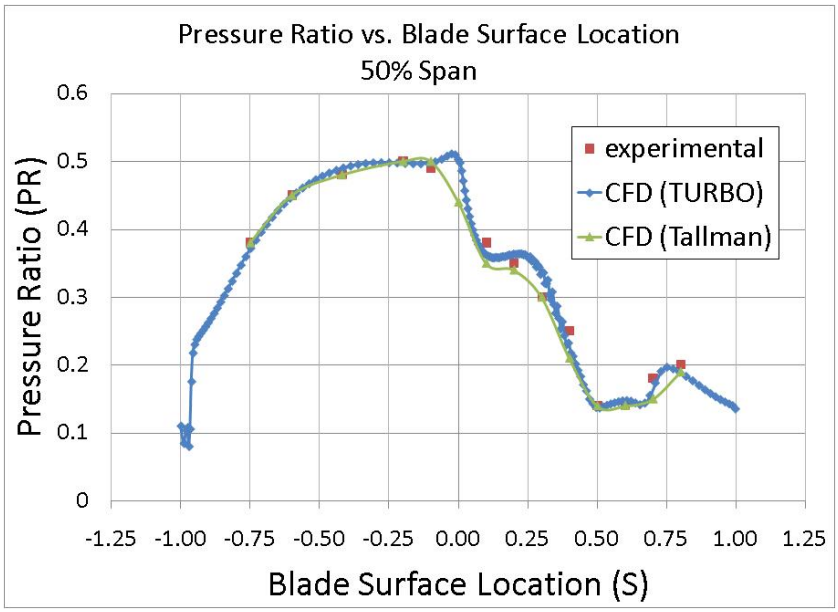

Figure 8.8: Blade Pressure Distribution at 50% Span

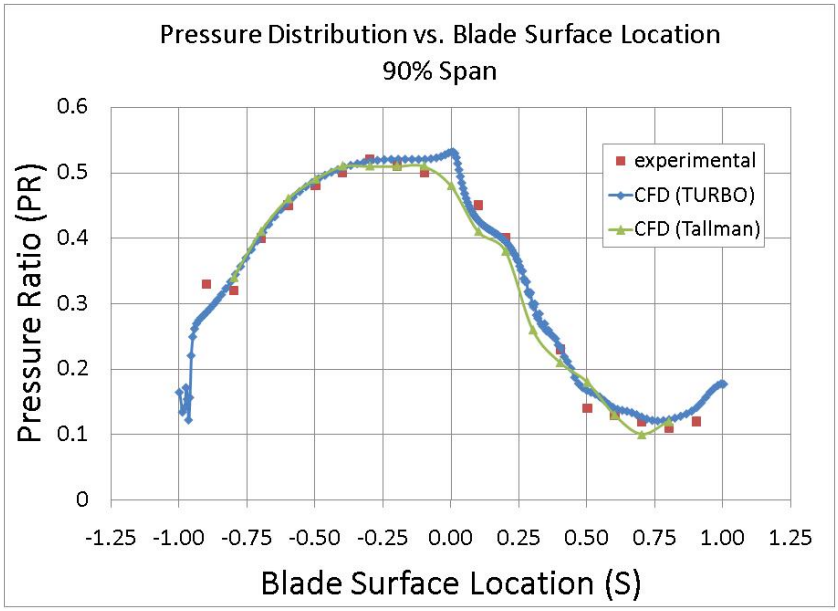

Figure 8.9: Blade Pressure Distribution at 90% Span

The differences in the pressure distribution on the pressure side of the blade at different spanwise locations indicate that the pressure distribution is three-dimensional. This can be clearly shown with a display of the pressure contours on the suction and pressure surfaces of the rotor blade. Notice the increased pressure at the leading edge near the hub (Figure 8.10 and Figure 8.11).

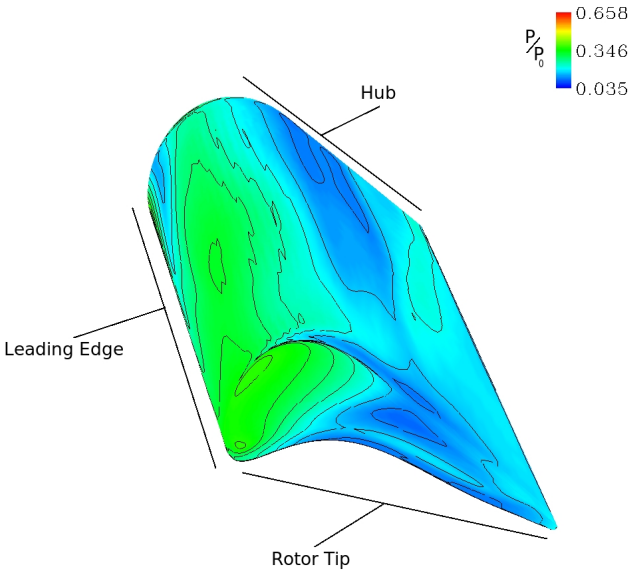

Figure 8.10: Blade Surface Pressure Contours (Suction Side; Relative Frame)

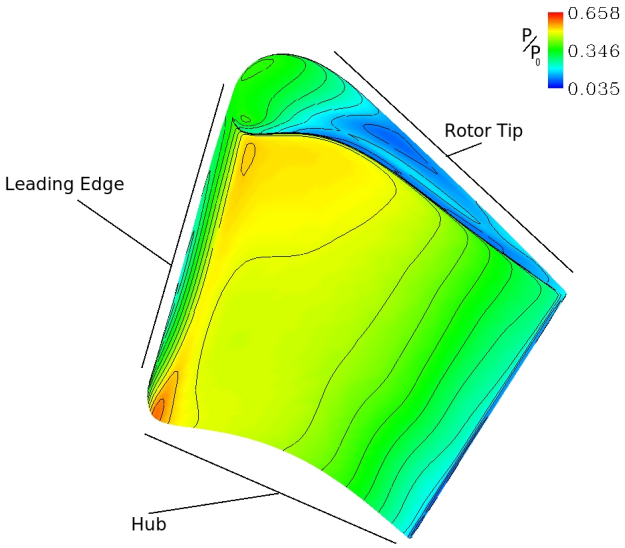

Figure 8.11: Blade Surface Pressure Contours (Pressure Side;Relative Frame)

8.3.2 Blade Surface Heat Transfer

Heat transfer at the leading edge of the blade is quite high (Figure 8.12). Reading literature on the reason behind this effect reveals that this is actually a well-documented fluid dynamics phenomenon, called the horseshoe-vortex. The horseshoe vortex affects the blade heat transfer on the hub and on the leading edge near the hub. This phenomenon is the result of endwall boundary layer flow stagnating against the airfoil leading edge (Schlichting [29]). This stagnating endwall boundary layer results in a radial pressure gradient. The airfoil surface fluid is then drawn toward the endwall due to the radial pressure gradient at the leading edge. Freestream fluid at high-temperature fills the void left by the airfoil surface fluid that has migrated to the endwall. This leads to increased heat transfer. Unfortunately, the experimental data does not reveal this flow feature because this phenomenon is confined to the bottom 10% span of the blade. However, Tallman's CFD predictions at 15% span show that the ST values in close proximity to the leading edge are high (Tallman p.7,15[34]). The predictions in the CFD simulation revealed similar results to the computations by Tallman et al. [34]. The horseshoe vortex phenomenon is further evidenced by the Stanton number graphs at three spanwise locations (Figures 8.16, 8.17, and 8.18). The heat transfer is greatest at the leading edge at all three spanwise graphs. However, the Stanton number at the leading edge at the 15% span location (Figure 8.16) is 25% greater than the Stanton numbers at the leading edge at the 50% and 90% span locations (Figure 8.17 and Figure 8.18). A horseshoe vortex schematic is given in Figure 8.14.

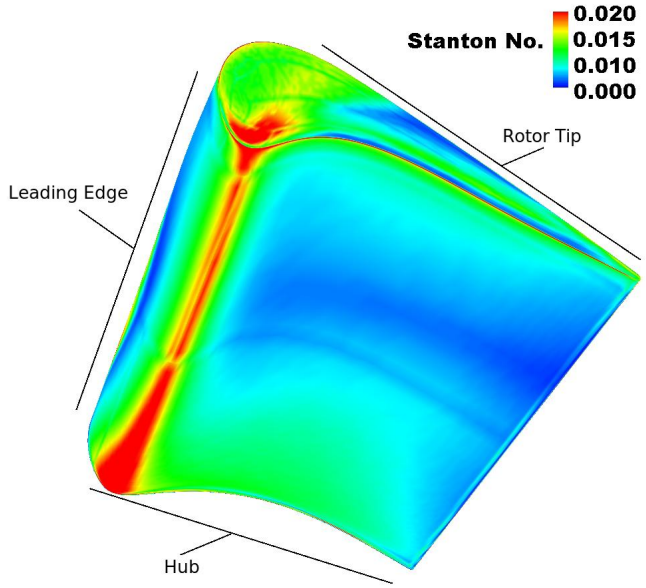

Figure 8.12: Blade Stanton Number Contours (pressure side)

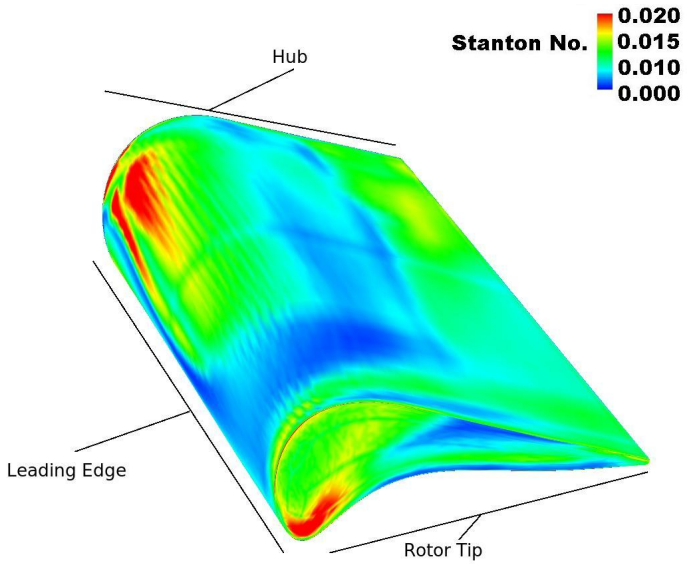

Figure 8.13: Blade Stanton Number Contours (suction side)

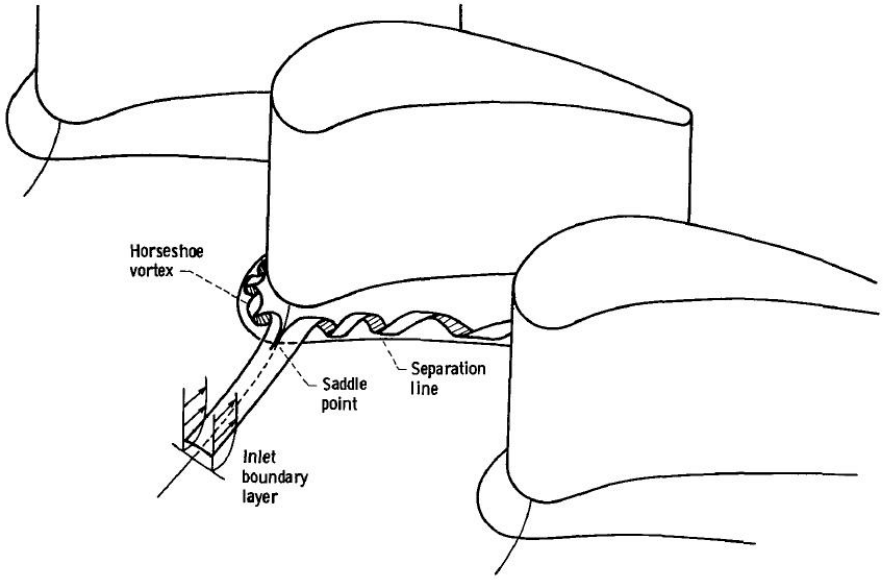

Figure 8.14: Horseshoe Vortex Schematic(Gaugler et al. [38])

Once again, the presence of the shock can be seen at S=0.7 at 15% and 50 % span in Figures 8.16 and 8.17. This is proven by looking at the Mach number and the heat transfer in that region. The shock is evidenced by looking at the change in Mach number from over one to a Mach number of under one. In order for the Mach number change to be a valid support for the evidence of a shock, the change must occur outside the boundary layer. The velocity profile (Figure 7.3) indicates the thickness of the boundary layer. The Mach number at 50% span is plotted in Figure 8.15, which displays the change in Mach number over one to a Mach number under one indicating a shock at S=0.7. The pressure jump and heat transfer jump help to support the existence of a shock at that location.

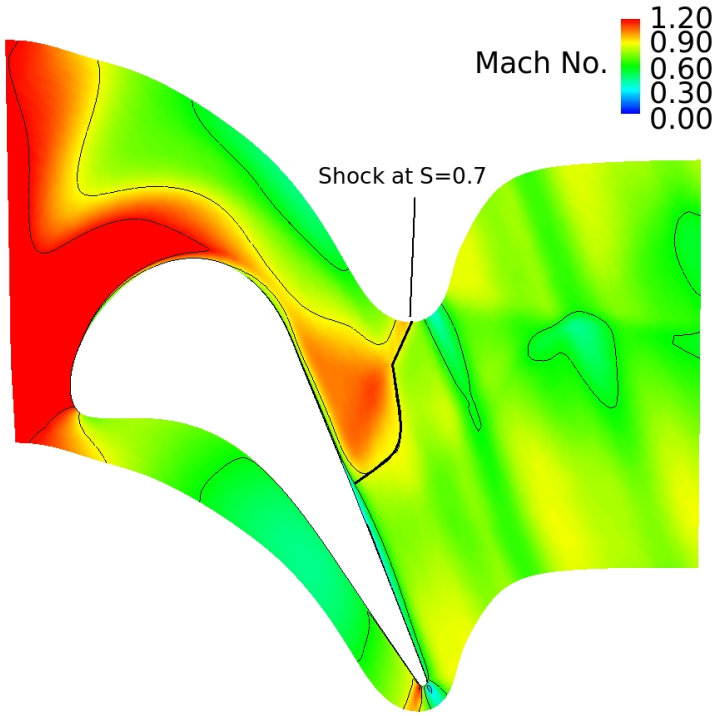

Figure 8.15: Mach No. at 50% span (Relative Frame)

The shock causes a jump in heat transfer in Figure 8.16 and in Figure 8.17. This sudden increase in heat transfer is the result of the trailing edge of a shock interacting with the boundary layer on the suction side blade surface. The experimental data unfortunately does not capture this effect in detail because there is little data in that region. In the experimental data a shock is indicated by the jump in heat transfer at 15% span around S = 0.7 (Figure 8.16). The heat transfer computations matches fairly well with the measurements on the pressure side of the blade. The heat transfer results match well on the suction side at 15% span from S=0 to S=0.75. However, for the last quarter of the suction side of the blade surface, the predictions are significantly

higher than the experimental data. The 50% span graph is displayed in Figure 8.17. The suction side predictions at 50% span heat transfer is lower than the experimental data. The 90% span results are shown in Figure 8.18. The suction side predictions of the heat transfer at 90% span from S=0.75 to S=1 are significantly larger than the experimental data. The mismatches between steady computational predictions and experimental data on the suction side is consistent with Ameri et al. [10] observations. They discovered significant heat transfer differences on the suction side of the blade near the hub and near the tip region between steady and time-averaged results from an unsteady analysis.

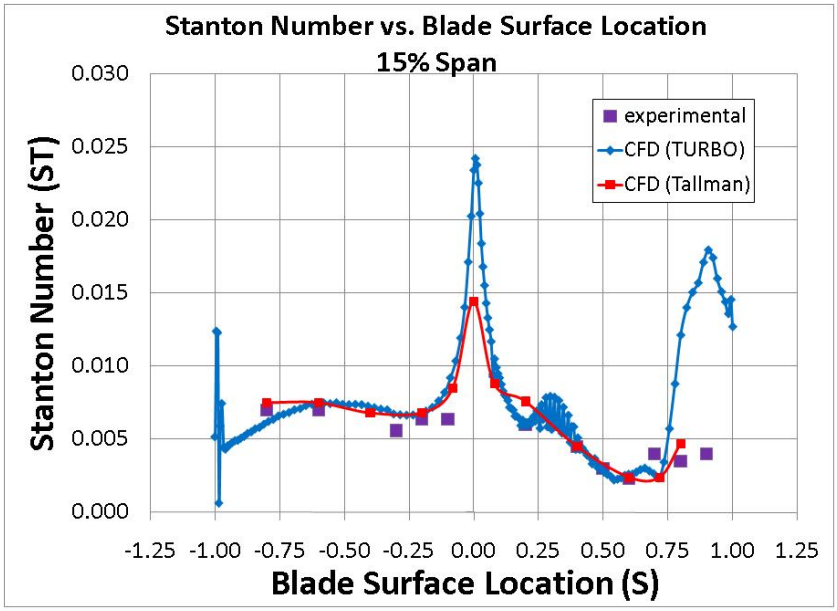

Figure 8.16: Blade Stanton No. at 15% Span

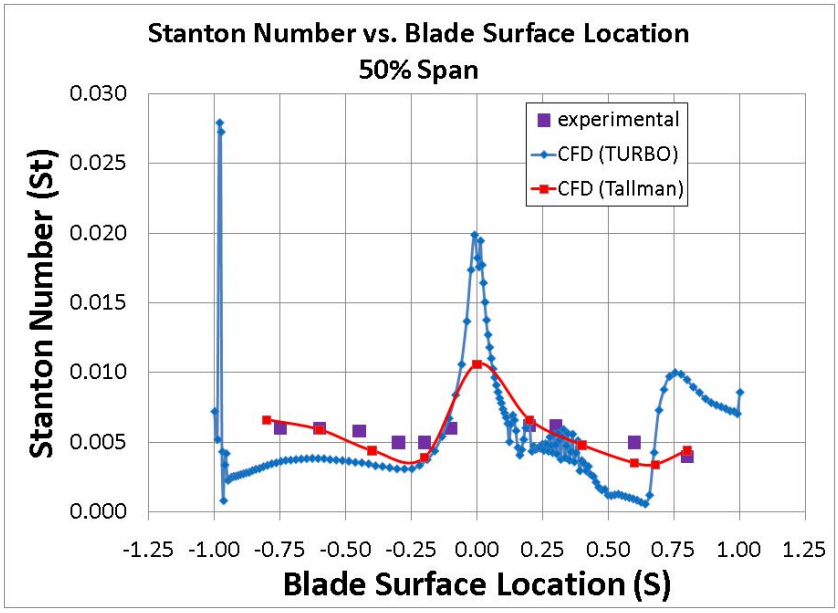

Figure 8.17: Blade Stanton No. at 50% Span

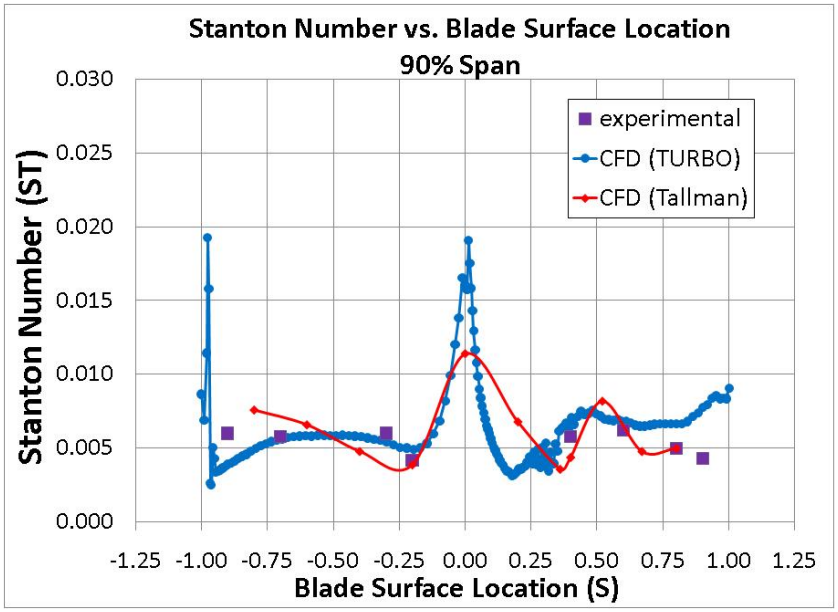

Figure 8.18: Blade Stanton No. 90% Span

The convergence of the heat transfer results are confirmed by comparing successive iterations of 5000 (Figure 8.19) .

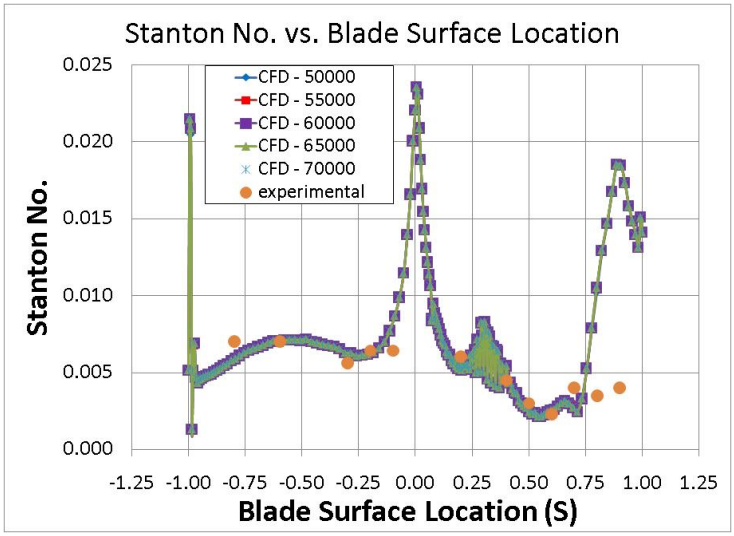

Figure 8.19: Convergence of blade surface heat transfer at 15% span

This steady-state computation has not taken into account the unsteady effect of wake passing on transition (Ameri and Arnone [5]). Figure 8.20 is a plot of percent error between the computation results and the experimental data. The discrepancies at S<-0.9 and S>0.6 are not displayed here. The percent error at those locations vary greatly and the computational results did not match up well with the experimental data. The largest percent difference in Figure 8.20 is 25% which occurs near the trailing edge. The percent error is calculated with the following formula:

$$percent\ error = \frac{CFD - experimental}{experimental} \times 100\%$$

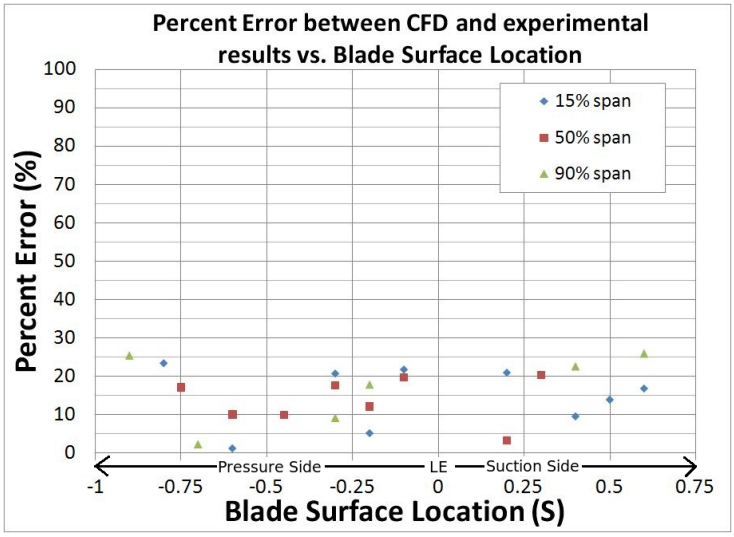

Figure 8.20: Stanton No. Percent Error vs. Blade Surface Location

8.3.3 Rotor Endwall Heat Transfer

The Stanton Numbers on the blade hub, blade casing, and blade tip are presented in Figures 8.22 and 8.25 and displays the locations where measurements were taken. Two experimental sets of data from Haldeman [24], a set of predictions from Tallman et al. [34], and TURBO's computation are presented together for comparison in Figures 8.23 and 8.26. The computation performed for this thesis has good agreement with both experimental data and computational results. The predictions made by TURBO had better agreement with the experimental data at probes 1,2,3,4,8,9, and 10. However, at probes 5,6, and 7, Tallman's computation had better agreement with the experimental data. The region where TURBO's computation were not as accurate is near the pressure side of the blade surface. The largest discrepancy occurs at probe 7. However, probe 7's experimental data is questionable because it is at a location very near

probe 5 and 6, yet the heat transfer difference between probes 5 and 6 with probe 7 is quite large. Also, it is in a region where the heat transfer is not changing quickly. In general both computations, Tacoma's simulation by Tallman et al. [34] and TURBO's predictions of heat transfer, were significantly elevated over the experimental results. The two different experimental data sets are two different runs with the same operating conditions (Figure 8.23). There is a small degree of uncertainty in the experimental results.

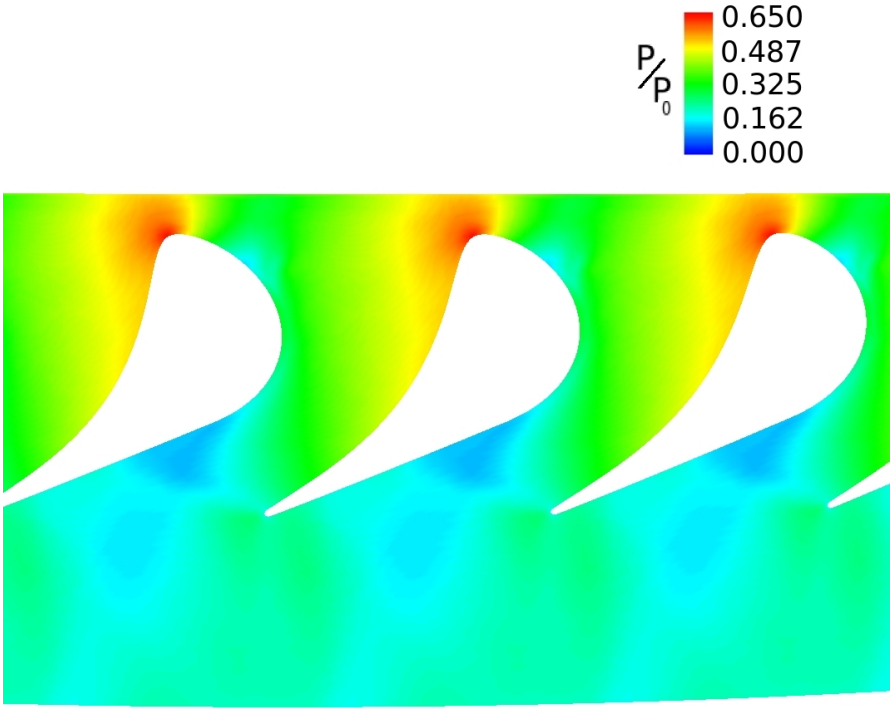

Figure 8.21: Rotor Hub Pressure Contours

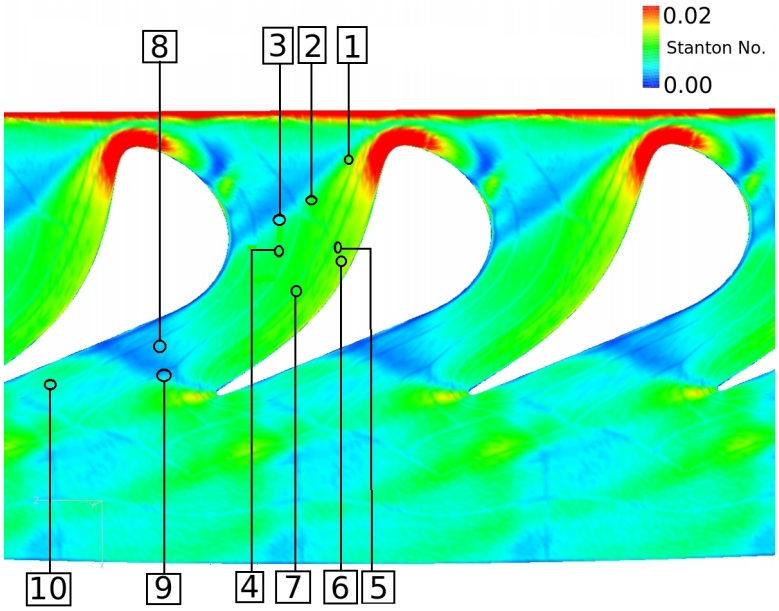

Figure 8.22: Rotor Hub Endwall ST Contours

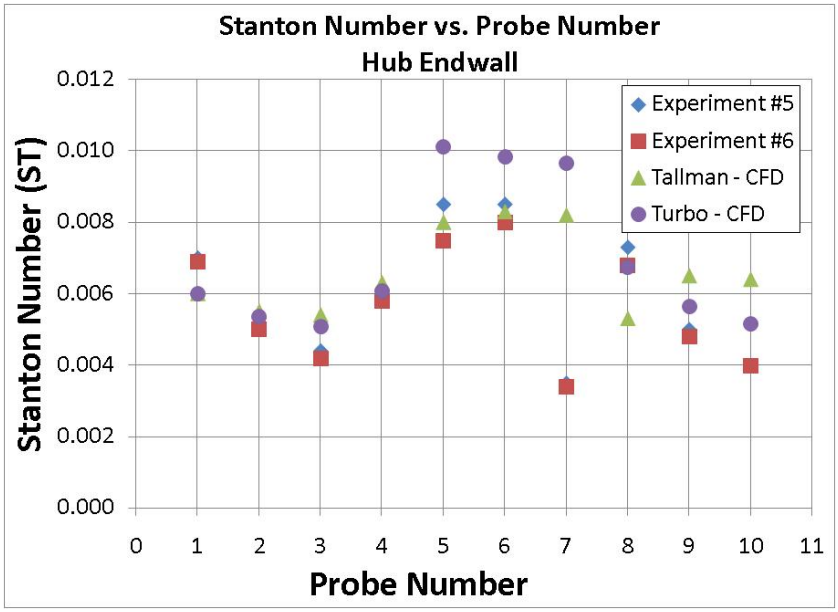

Figure 8.23: Rotor Hub Stanton No. Graph

Tallman did not compute heat transfer predictions for the casing of the rotor. The casing heat transfer is significantly greater than the rotor tip heat transfer. The rotor tip leakage flow results in increased heat transfer on the casing surface especially near the pressure side and the leading edge of the blade region. This does not agree with the experimental results by Thorpe et al. [36] which indicated that the regions of highest heat flux on the casing surface occurs in the region near the suction side of the blade. However, the experimental results of Epstein et al. [19] and the computational predictions of Ameri and El-Gabry [7] indicate the peak heat flux occurring in the region near the pressure side of the rotor tip region. Further investigation of the results from TURBO would be needed in order to determine the amount of increased heat flux that the leakage is responsible for. Thorpe et al. [36] performed experiments investigating the effect of the rotor tip on the casing heat load of a transonic axial flow turbine. They discovered that 50% of the casing heat transfer was a result of the rotor tip leakage flow in the region of 35% to 60% axial chord. Then Ameri and El-Gabry [7] performed unsteady CFD computations on the heat transfer for the casing of a turbine blade. Their CFD analysis was in good agreement the experimental results of Epstein et al. [19] and did not agree with the conclusions of Thorpe et al. [36]. Ameri and El-Gabry ([7], p. 6) suggest that the location of the peak heat flux on the casing surface is dependent upon airfoil geometry and pressure distributions in the rotor gap region. The suggestion that the heat transfer distribution is connected to the pressure distribution is demonstrated cleary in TURBO's computation for the hub surface by comparing Figure 8.21 and 8.22. This effect is shown for the casing of the rotor by comparing Figures 8.24 and 8.25.

Also, Ameri and El-Gabry [7] found that the effect of unsteadiness due to wake

passing had a significant impact on the casing heat transfer results. Their unsteady results were 16.8% higher than the steady CFD results.

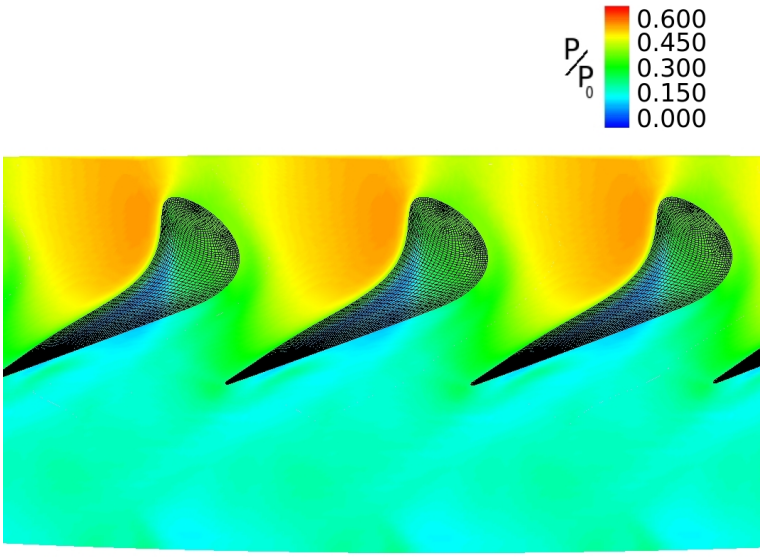

Figure 8.24: Rotor Casing Pressure Contours

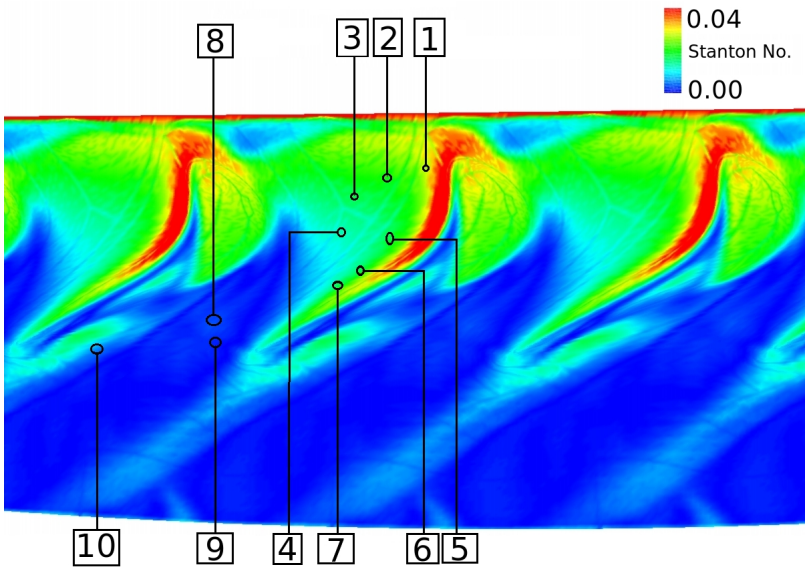

Figure 8.25: Rotor Casing Endwall ST Contours

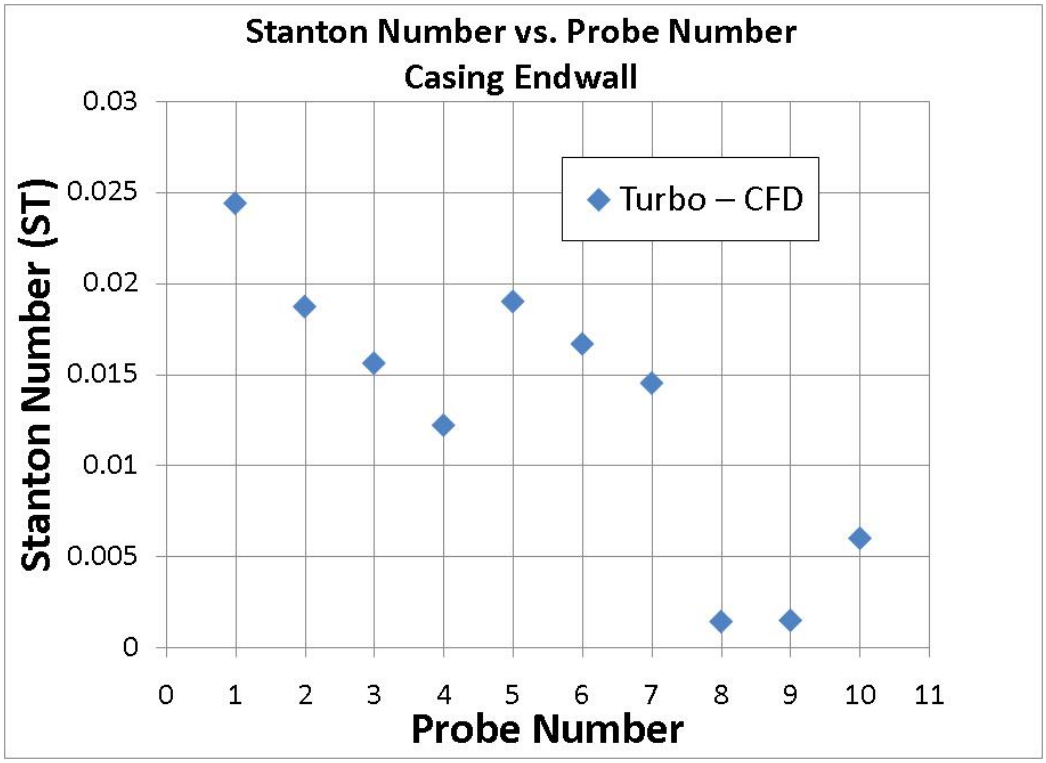

Figure 8.26: Rotor Casing Stanton No. Graph

8.3.4 Rotor Tip Heat Transfer

Figure 8.29 displays the heat transfer distribution in non-dimensionalized Stanton numbers and it also indicates the locations of the four probes. Figure 8.29 is a graph comparing experimental data (Haldeman et al. [24]), Tallman et al. [34] computation, and TURBO's computational results for the rotor tip heat transfer. The agreement between rotor tip predictions and experimental data is only fair. The general trend shown in the experimental data of increases and decreases in heat transfer was captured well by the computation. However, the Stanton number values of the computation is on average 26.5% greater than the experimental data. This is consistent with the CFD

computation by Molter et al. [28] which resulted in an over prediction of 25% percent over the experimental data. All of the CFD results from Tallman et al. [34] lie outside of the scatter of experimental data. For the TURBO computation, the results at probe 4 lie within the scatter of experimental data. While probes 1,2, and 3 lie outside of the experimental data. The largest discrepancy is at probe 3. This is a region where the rate of change of the heat transfer is high, so points nearby the location of the probe may be significantly different in value. Also, the heat transfer in the rotor tip region is not universal for all turbines. The heat transfer in this region is influenced by the airfoil geometry and pressure distributions (Section 8.3.3). If the measurement at probe 3 is ignored, the average difference between the computation by TURBO and experimental results at probes 1,2, and 4 is 15.5%. Figure 8.28 is a display of the rotor tip with contour lines which represent lines of constant Stanton number. Notice that the contour lines are generally smooth which is evidence that the flowfield has converged.

Ameri and Bunker [2] found that the assumption of periodic flow as not valid for the calculation of blade tip heat transfer. So, the entire passage would need to be modeled in order for a valid computation of the blade tip heat transfer to be achieved. Also, an unsteady computation with the effect of wake passing should also be included in order to obtain more accurate results.

There is increased heat transfer near the leading edge on the tip surface. This is explained by the scrubbing of the tip vortex (Ameri, et al. [10]). This is a result of the acceleration of high-temperature freestream fluid from the passage into the tip clearance gap. The high-temperature fluid also increases the heat transfer on the tip surface downstream of the leading edge (Figure 8.27).

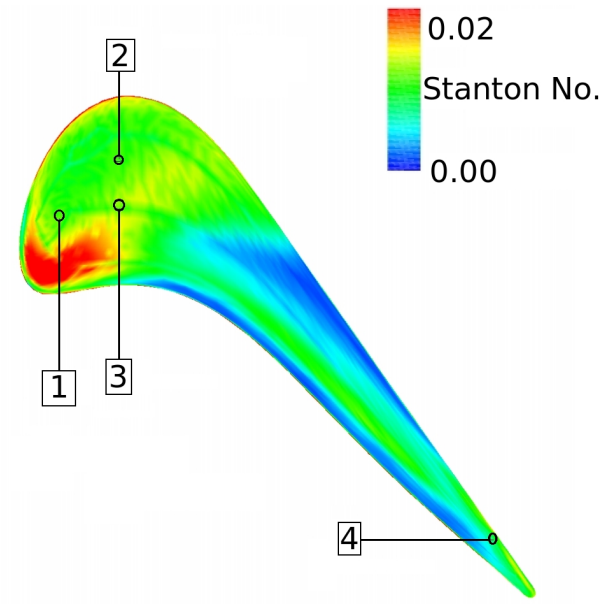

Figure 8.27: Steady Rotor Tip Stanton Number Contours

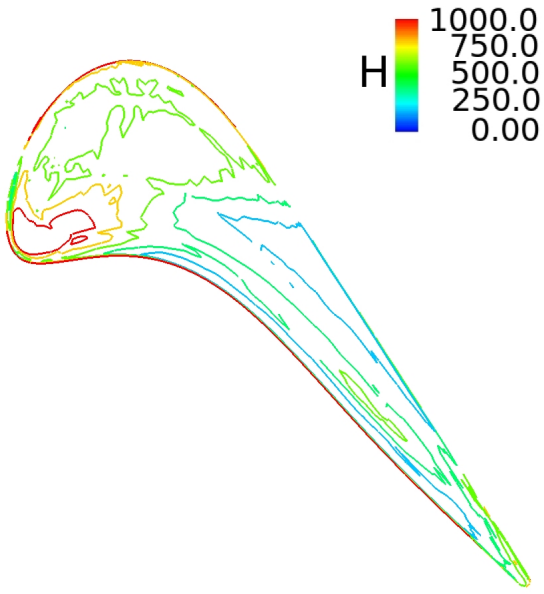

Figure 8.28: Steady Rotor Tip Stanton Contour Lines

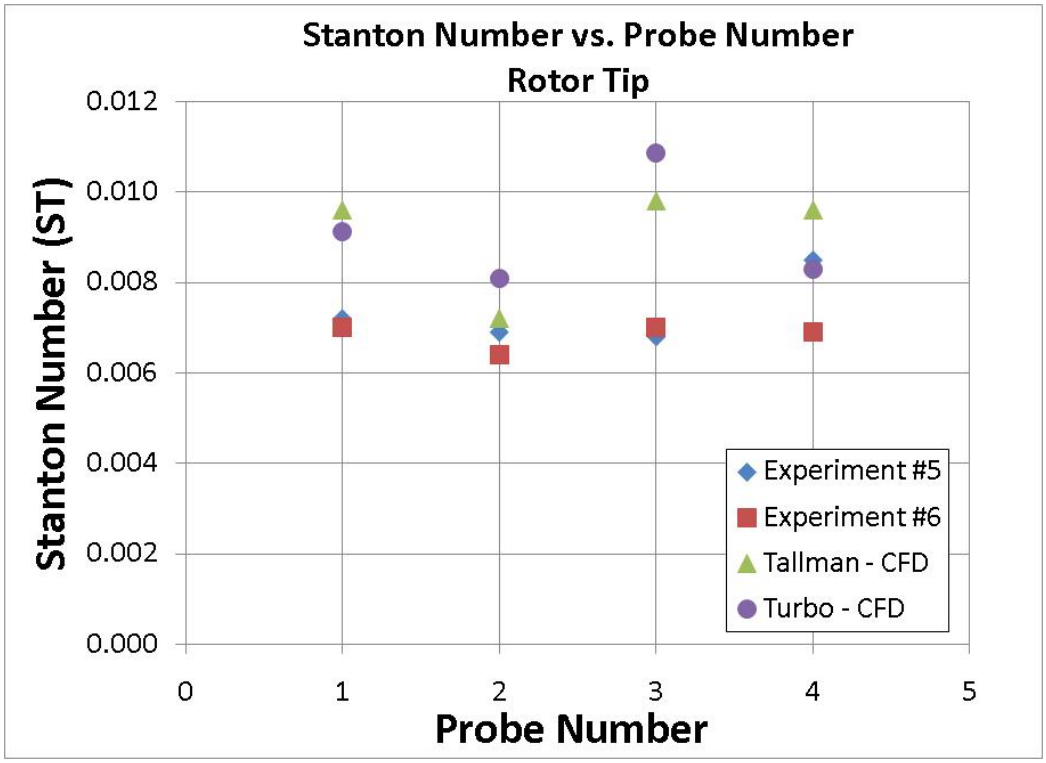

Figure 8.29: Rotor Tip Stanton Number Graph

8.4 Experimental Error

There are a few areas where the CFD predictions do not match exactly with the experimental data. The reason behind these inconsistencies can be one of several. The most likely reason for the mismatch in prediction and data would come from the method of recovering data from FieldView. Fieldview was used to view and extract pressure data from the CFD code. In order to simplify calculations, a slice of pressure data was taken at a constant index location along the surface of the vane. Haldeman [24] talks about measurement uncertainty and bounding the uncertainty for the experimental data.

CHAPTER 9

CONCLUSIONS

The main objective of this thesis was to compare TURBO's CFD results with previous computations and experimental data from a rig. The quality of the grid used in this thesis can be measured by how well the computations compare with experimental data. Comparisons of pressure distributions and heat flux were made for both blade rows. For the stator vane, the pressure distribution predictions had excellent agreement with the experimental data produced by Haldeman [24]. The heat transfer predictions were within the scatter of experimental data with only a few exceptions.

For the rotor blade predictions, the pressure predictions at all three spanwise locations had good agreement with the experimental results by Haldeman [24]. The overall trend in heat flux predictions were similar to the experimental data. On the rotor blade surface, the heat flux predictions matched well and the largest percent error between the computation and the experimental data was 25%. The heat transfer predictions were good from S=0 to S=0.6 location on the suction side and from S=0 to S=-0.9 on the pressure side. So, the computations were fairly accurate up to three quarters of

the blade. The peak heat flux predictions were at the leading and trailing edge which is expected. However, experimental data at those specific points were unavailable for comparison.

The predictions for the hub endwall of the rotor were good except for the region near the pressure side of the blade. The percent error between computational results and experimental data was on average 13.1% greater.

The heat transfer predictions in the rotor tip region was expected to be higher than the experimental results by Haldeman [24], because the tip clearance of the grid used in this thesis was slightly larger. The CFD predictions for the rotor tip heat transfer had good agreement with previous computational predictions by Tallman et al. [34], but only fair agreement with the experimental data. The rotor tip predictions for heat transfer were on average 26.5% greater than the experimental measurements. The location of peak heat flux in the rotor tip region varies from experiment to experiment. The rotor tip predictions were only 15.5% greater than the experimental results. The discrepancies between the computational results and the experimental data concerning the location of peak heat flux on the casing surface of the turbine were discussed in this thesis.

Flow-physics were influenced by the geometry and the flow-field in the turbine rotor blade. The good agreements between computational results and experimental data gives more confidence in the use of CFD for testing and for design purposes. The results presented in this thesis increases the knowledge and understanding of heat transfer in a turbine. The computational results were able to reveal some areas on the rotor blade that had high levels of heat transfer which were not revealed by the experimental results. Knowing the location of the highest heat loads being applied to

the turbine blade can lead to better design. Computational flow solvers will continue to benefit the turbo-machinery world.

BIBLIOGRAPHY

[1] Ameri, A. A., Steinthorsson, E., Rigby, D. L., "Effect of Squealer Tip on Rotor Heat Transfer and Efficiency," Journal of Turbomachinery, vol. 120, No. 4, Oct. 1998, pp. 753-759.

[2] Ameri, A. A., Bunker, R., S., "Heat Transfer and Flow on the First-Stage Blade Tip of a Power Generation Gas Turbine: Part 2 - Simulation Results," ASME Journal of Turbomachinery, 122, pp. 272-277, Apr. 2000.

[3] Ameri, A. A., "Heat Transfer and Flow on the Blade Tip of a gas Turbine Equipped with a Mean-Camberline Strip," ASME Journal of Turbomachinery, 123, No. 4. pp. 704-708, October 2001.

[4] Ameri, A. A., E. Steinthorsson, D. Rigby, "Effect of Tip Clearance and Casing Recess on Heat Transfer and Stage Efficiency in Axial Turbines," ASME Journal of Turbomachinery, 121, No. 4, pp 683-693, October 1999.

[5] Ameri, A. A., A. Arnone, "Transition Modeling Effects on Turbine Rotor Heat Transfer," ASME Journal of Turbomachinery, 118, No. 2, pp. 307-313, Apr. 1996.

[6] Ameri, A.A., P.M. Sockol and R.S.R Gorla, "Navier-Stokes Analysis of Turbomachinery Blade External Heat Transfer," AIAA Journal of Propulsion and Power, 8, Nov. 1992.

[7] Ameri, A. A., El-Gabry, L., "Computation of Unsteady Heat Transfer on the Casing of a Turbine Blade," 12th International Symposium on Transport Phenomena and Dynamics of Rotating Machinery. Honolulu, Hawaii, February 17-22, 2008. ISROMAC12-2008-20191, 2008.

[8] Ameri, A.A., Rigby, D. L., Steinthorsson, E., Heidmann, J., Fabian, J. C., "Unsteady Analysis of Blade and Tip Heat Transfer as Influenced by the Upstream Momentum and Thermal Wakes," ASME TURBO Expo 2008: Power for Land, Sea, and Air, June 9 -13, 2008. Berlin, Germany. GT2008-51242.

[9] Ameri, A. A., Rigby, D., Heidmann, J. Steinthorsson, E., Fabian, J., “Effects of Unsteadiness Due to Wake Passing on Rotor Blade Heat Transfer,” ASME Joint Thermophysics and Heat Transfer Conference. June 2006, San Francisco, California. AIAA-2006-3263.

[10] Ameri, A. A., Rigby, D., Heidmann, J., Steinthorsson, E., Fabian, J., “Unsteady Turbine Blade and Tip Heat Transfer Due to Wake Passing,” International Gas Turbine Institute. ASME TURBO Expo 2007: Power for Land, Sea and Air. May 2007, Montreal, Canada. GT2007-27550.

[11] Barrows, S.T., ”TURBO Turbulence Model Validation with Recommendations to Tip-Gap Modeling,” B.S.M.E Thesis in the Department of Aeronautical and Astronautical Engineering, 2008, Ohio State University: Columbus.

[12] Boyle, R.J., Ames, F.E., Giel, P.W., “Predictions for the Effects of Freestream Turbulence on Turbine Blade Heat Transfer,” ASME TURBO Expo 2004: Power for Land, Sea, and Air. June 14-17, 2004, Vienna, Austria. GT-2004-54332.

[13] Chana, K., S., Singh, U., K., Povey, T., “Turbine Heat Transfer and Aerodynamic Measurements and Predictions for a 1.5 Stage Configuration,” ASME TURBO Expo 2004: Power for Land, Sea, and Air. June, 2004. Vienna, Austria. GT2004-53951.

[14] Chand, K. K., Lee, K. D., “TURBO machinery Blade Optimization Using the Navier-Stokes Equations,” ASME TURBO Expo 2004: Power for Land, Sea, and Air. June14-17, 2004, Vienna, Austria. GT2004-53951.

[15] Chen, J., P., “Unsteady Three-Dimensional Thin-Layer Navier-Stokes Solutions for Turbomachinery in Transonic Flow,” Ph.D. Dissertation in the Department of Aerospace Engineering, 1991, Mississippi State University: Mississippi State.

[16] Chen, J.P., Ghosh, A.R., Sreenivas, K, Whitfield, D.L., “Comparisons of Computations using Navier-Stokes Equations in Rotating and Fixed Coordinates for Flow through Turbomachinery,” AIAA Paper No. 97-0878, 1997.

[17] Chien, K.Y. "Predictions of Channel and Boundary-Layer Flows with a Low-Reynolds Number Turbulence Model", AIAA Journal, Vol. 20, No. 1, pp. 33-38.1982.

[18] Davis, R., L., Yao, J., Clark, J., P., Stetson, G., Alonso, J., J., Jameson, A., Haldeman, C., W., Dunn, M., G., “Unsteady Interaction Between a Transonic Turbine Stage and Downstream Components,” International Journal of Rotating Machinery. p.495-506, 2004.

[19] Epstein, A.H., Guenette, G.R., Norton, R.J.G, and Yuzhang, C., "Time Resolved Measurements of a Turbine Rotor Stationary Tip Casing Pressure & Heat Transfer Field," AIAA Paper 85-1220, July 1985.

[20] Galassi, L., King, P., Elrod, W., "Effects of Inlet Turbulence Scale on Turbine Blade Surface Heat Transfer in a Linear Cascade," AIAA Paper No. 90-2264, 1990.

[21] Green, B.R., "Time-Averaged and Time-Accurate Aerodynamics for the Recessed Tip Cavity of a Rotating High-Pressure Turbine Blade and the Stationary Outer Shroud," B.S.M.E. Thesis in the Department of Aerospace Engineering, 2004, Ohio State University: Columbus.

[22] Haldeman, C.W., Mathison, R.M., Dunn, M.G., Southworth, S., Harral, J.W., Heitland, G., "Aerodynamic Heat Flux Measurements in a Single Stage Fully Cooled Turbine - Part II: Experimental Results,"ASME TURBO Expo 2006: Power for Land, Sea, and Air. May 8-11, 2006, Barcelona, Spain. GT2006-90968.

[23] Haldeman, C. W., Dunn, M.G., Barter, J.W., Green, B.R., Bergholz, "Aerodynamic and Heat-flux Measurements with Predictions on a Modern One and 1/2 Stage High Pressure Transonic Turbine," Journal of Turbomachinery, 2004. Vol. 127:p.522-531.

[24] Haldeman, C.W., "An Experimental Investigation of Clocking Effects on Turbine Aerodynamics Using a Modern 3-D One and one-half Stage High Pressure Turbine for Code Verification and Flow Model Development," Ph.D Dissertation in the Aeronautical and Astronautical Engineering, 2003, Ohio State University: Columbus.

[25] Haldeman, C.W., Dunn, M.G., "Heat Transfer Measurements and Predictions for the Vane and Blade of a Rotating High-Pressure Turbine Stage." ASME TURBO Expo 2003: Power for Land, Sea, and Air. June 16-19, 2003, Atlanta, Georgia.

[26] Han, J., "Turbine Blade Cooling Studies at Texas A&M University: 1980-2004," Journal of Thermophysics and Heat Transfer, Vol. 20, No. 2, April-June 2006. p. 161-187.

[27] Kwak, J. S., and Han, J. C., 2003, "Heat Transfer Coefficient on a Gas Turbine Blade Tip and Near Tip Regions," presented at the 8th AIAA/ASME Joint Thermophysics and Heat Transfer Conference, St. Louis, June, Paper No. AIAA-2002-3012

[28] Molter, S., M., Dunn, M., G., Haldeman, C., W., Bergholz, R., F., Vitt, P., "Heat-Flux Measurements and Predictions for the Blade Tip Region of a High-Pressure Turbine," ASME TURBO Expo 2006: Power for Land, Sea and Air. May, 2006. GT2006-90048.

[29] Schlichting, H., Boundary Layer Theory, 8th ed. 2000: McGraw-Hill Book Company.

[30] Shabbir, A., Zhu, J., Celestina, M., "Assessment of Three Turbulence Models in a Compressor Rotor," ASME Paper No. 96-GT-198, June, 1998.

[31] Shih, T.h., Liou, W.W., Shabbir, A., Yang, Z., and Zhu, J., 1995, "A New $\kappa - \varepsilon$ Eddy Viscosity Model for High Reynolds Number Turbulent Flows," Computers Fluids, Vol 24, No 3., pp. 227-237.

[32] Suryanarayanan, A., Mhetras, S., P., Schobeiri, M., T., Han, J., C., "Film-Cooling Effectiveness on a Rotating Blade Platform," ASME TURBO Expo 2006: Power for Land, Sea and Air. May 8-11, 2006. Barcelona, Spain. GT2006-90034.

[33] Tallman, J., A., "CFD Heat Transfer Predictions for a High-Pressure Turbine Stage," ASME TURBO Expo 2004: Power for Land, Sea, and Air. June 14-17, 2004. Vienna, Austria. GT2004-53654.

[34] Tallman, J.A., Haldeman, C. W., Dunn, M. G., Tolpadi, A. K., Bergholz, R. F., "Heat Transfer Measurements and Predictions for a Modern, High-Pressure, Transonic Turbine, Including Endwalls," ASME TURBO Expo 2004: Power for Land, Sea, and Air. June 14-17, Vienna, Austria. GT2006-90927.

[35] Tallman, J. A., "A Computational Study of Tip Desensitization in Axial Flow Turbines Part 1: Baseline Turbine Computations and Comparisons with Measurement," ASME TURBO Expo 2004: Power for Land, Sea, and Air. June, 2004. GT-2004-53918.

[36] Thorpe, S.J., Miller, R.J., Yoshino, S., Ainsworth, R.W., Harvey, Neil W., "The Effect of Work Processes on the Casing Heat Transfer of a Transonic Turbine," GT2005-68437, June 2005.

[37] Zhu, J., Shih, T.H., "An NPARC Turbulence Module with Wall Functions," Tech. rep., NASA, Institute for Computational Mechanics in Propulsion and Center for Modeling of Turbulence and Transition, ICOMP, NASA Lewis Research Center, Cleveland, O.H., August 1997, AIAA Paper No. 1996-0382; NASA-CR-204143; ICOMP-97-10; CMOTT-97-05.

[38] Gaugler, R.E., Russell, L.M., ”Flow Visualization Study of the Horseshoe Vortex in a Turbine Stator Cascade”, NASA Technical Paper No. 1884, 1984, Cleveland, Ohio.

APPENDICES

TURBO Core Model

TURBO is a three dimensional, time-accurate, compressible fluid code based on the Reynolds Averaged Navier Stokes equations (RANS). The RANS equations are represented in tensor form (for simplification) in equations 9.1 (conservation of mass),9.2 (conservation of momentum), and 9.3 (conservation of energy) (These equations are from Chen et al. [16] and Barrows [11]).

$$\frac{\partial \rho}{\partial t} + \frac{\partial}{\partial x_j}\left[\rho(u_j - V_j)\right] = 0 \tag{9.1}$$

$$\frac{\partial \rho u_i}{\partial t} + \frac{\partial}{\partial x_j}\left[\rho(u_j - V_j)u_i + p\delta_{ij} - \tau_{ij}\right] = S_i \tag{9.2}$$

$$\frac{\partial E_t}{\partial t} + \frac{\partial}{\partial x_j}\left[(u_j - V_j)(E_t + p) - u_\iota \tau_{ij} - q_j\right] = 0 \tag{9.3}$$

V_i, velocities in the rotating frame, are represented in vector form in terms of 3 fixed frame components:

$$\vec{V} = \vec{\Omega} \times \vec{r} = \begin{bmatrix} V_1 \\ V_2 \\ V_3 \end{bmatrix} = \begin{bmatrix} 0 \\ -\Omega r_z \\ \Omega r_y \end{bmatrix} \tag{9.4}$$

S_i, source terms in the rotating frame , are also represented in vector form in terms of 3 fixed frame components:

$$\vec{S} = \begin{bmatrix} S_1 \\ S_2 \\ S_3 \end{bmatrix} = \begin{bmatrix} 0 \\ -\rho w \Omega \\ \rho v \Omega \end{bmatrix} \tag{9.5}$$

The laminar and thermal conductivities are represented by k_{lam} and k_{turb} respectively with the heat flux terms q_j, given by

$$q_j = -(\kappa_{lam} + \kappa_{turb})\frac{\partial T}{\partial x_j} \tag{9.6}$$

The shear stress is a combination of a laminar and a turbulent component. Using tensor rules for the shear stress tensor, the laminar and turbulent designations are moved to superscripts.

$$\tau_{ij} = \tau_{ij}^{lam} + \tau_{ij}^{turb} \tag{9.7}$$

$$\tau_{ij}^{lam} = 2\mu_{lam}\left(S_{ij} - \frac{1}{3}S_{ij}\delta_{ij}\right) \tag{9.8}$$

where μ_{lam}, the laminar viscosity is given by Sutherland's formula:

$$\mu_{lam} = \mu_0 \frac{T_0 + C}{T + C}\left(\frac{T}{T_0}\right)^{3/2}$$

$$\tau_{ij}^{turb} = 2\mu_{turb}\left(S_{ij} - \frac{1}{3}S_{ij}\delta_{ij}\right) - \frac{2}{3}\rho k\delta_{ij} \tag{9.9}$$

where μ_{turb}, the turbulent viscosity is defined in equation **??**.

The rate of strain tensor is given:

$$S_{ij} = \frac{1}{2}\left(\frac{\partial u_i}{\partial x_j} + \frac{\partial u_j}{\partial x_i}\right) \tag{9.10}$$

Clustering

Clustering is a tool found in the GridPro application which allows a user to manipulate a grid to become fine near a surface. Clustering for this thesis was done at all physical surfaces. The following are the commands used for producing the meshes found in this thesis.

For the stator grid: clu stator.tmp -s 1 4e-5 1.1 -s 2 4e-6 1.1 -s 6 1e-5 1.1

For the rotor grid: clu rotor.tmp-s 4 1e-5 1.1 -s 3 1e-5 1.1 -s 5 1e-5 1.001

The commands above will be explained in order in Table 9.1.

parameters	description
clu	GridPro command: cluster
stator.tmp	GridPro grid file
-s	initiates surface clustering
1	clusters to surface with this id (hub)
4e-5	off-wall spacing
1.1	spacing growth ratio
-s	initiates clustering to another surface
2	cluster to casing
4e-6	off-wall spacing
1.1	spacing growth ratio
-s	initiates clustering to another surface
6	cluster to blade
1e-5	off-wall spacing
1.1	spacing growth ratio

Table 9.1: GridPro clustering commands

This step incorporates the use of the 'Cluster' command and produces a grid that with a higher grid point count. Also, the gridpoints in the radial direction have changed. However, the interface between the exit of the stator grid and the inlet of the rotor grid must match. So, the clustering process must be done with the result that the two blocks at the interface contain the same number of gridpoints in the radial direction.

Merging

Merging is another tool in GridPro which allows a user to reduce the number of blocks in a given grid. The 'merge' command uses complex mathematical algorithms to combine multiple blocks into one, while gridpoints remain unaltered. The merge command for the clustered stator grid is:mrgb stator.tmp.tmp

The merge command for the clustered rotor grid is:mrgb rotor.tmp.tmp

There are a few limitations for the merged grids in order for the interface matching code to work. The exit block of the stator grid and the inlet block of the rotor grid must be one complete block and not be separated into two smaller blocks. This is accomplished with the 'Merge' command. Once the merging functions have performed their tasks, then the blocks are ready to be taken through the interface matching code.

Welding

Welding is a command in GridPro which is useful for manipulating one or two blocks to match at the interface. The following is an example of how to conform exit.tmp to stator_exit.tmp: weld exit.tmp stator_exit.tmp -w 7 0 -1. The -w 7 0 part of the command tells GridPro to manipulate the exit.tmp block seven cells deep from the interface and to manipulate zero cells deep into the stator_exit.tmp block. The -1 at the end of the command indicates that the resulting grid that is produced only consist of the grids that have been manipulated, i.e. the exit block. The resulting grid is automatically named weld.tmp, so it should be renamed to statorweld.tmp. A similar command is used for the rotor inlet block: weld inlet.tmp rotor_inlet.tmp -p 2 2 -w 4 0 -1. The -p 2 2 part refers to the face that is to be matched. This can be done manually with the -p option or GridPro will automatically choose the face to weld if the -p option is not specified. The -w 4 0 refers to manipulating inlet.tmp only 4 cell deep and leaving the rotor_inlet.tmp grid as it is.

parameters	description
weld	GridPro command: weld
exit.tmp	grid file of exit block
stator_exit.tmp	grid file of temporary block
-w	define depth of manipulation
7	7 cells deep into exit block
0	do not manipulate temporary block
-1	output exit block only to weld.tmp

Table 9.2: Welding commands

Interface Matching Code

The interface matching code takes the exit block of the stator grid and the inlet block of the rotor grid and produces temporary grids for those two grids to be welded to. Comments have been inserted into the code.

```
program interface
implicit none
integer:: i,j,k,ni,nj,nk,nblks,nbmax,m,n
integer:: xdim,ydim,zdim,nbmax1,halfpt,halfpt1,iprime,kprime,jprime
integer:: xdim1,ydim1,zdim1,maxi,xdim1orig,start,end
real*16 leftpty, leftptz, centerpty, centerptz, rightpty, rightptz
```

```
real*16 bisect1y, bisect1z, bisect2y,bisect2z,leftslope,rightslope
real*16 bisect1slope, bisect2slope, constant1, constant2,rightptz1
real*16 leftpty1,leftptz1,centerpty1,centerptz1,rightpty1
real*16 bisect1y1,bisect1z1,bisect2y1,bisect2z1,leftslope1
real*16 rightslope1,centerptz2,centerpty2,temp1,temp2
real*16 intercept1,intercept2,z_intercept1,z_intercept2
real*16, dimension(:), allocatable:: leftslope2,rightslope2
real*16 bisect1slope1, bisect2slope1
real*16 hypot,angle,centerz2,centery2,PI,test1,test2
real*16 centerz, centery, radius, c, fullarc
real*16 centerz1,centery1
real*16, dimension(:), allocatable:: rad
real*16, dimension(:,:,:), allocatable:: x,y,z,xr,yr,zr
real*16, dimension(:,:,:), allocatable:: xtemp,ytemp,ztemp
real*16, dimension(:,:,:), allocatable:: xtemp1,ytemp1,ztemp1
real*16, dimension(:,:,:), allocatable:: xstore,ystore,zstore
real*16, dimension(:,:,:), allocatable:: xfinal,yfinal,zfinal
open(UNIT=7, FILE='exit.p3d', FORM='unformatted')
read(7) nbmax
read(7) xdim,ydim,zdim
C Reads dimensions of exit stator block
open(UNIT=9, FILE='stator_exit.p3d', FORM='unformatted')
write(9) 1
write(9) zdim,xdim,ydim
open(UNIT=8, FILE='inlet.p3d', FORM='unformatted')
read(8) nbmax1
read(8) xdim1,ydim1,zdim1
C Reads dimensions of inlet rotor block
open(UNIT=5, FILE='rotortemp.p3d', FORM='unformatted')
write(5) 1
write(5) xdim1,ydim1,zdim1
open(UNIT=4, FILE='rotor_inlet.p3d', FORM='unformatted')
write(4) 1
write(4) xdim1,ydim1,zdim1
PI = 3.14159265358979323846
m = 1
ni=xdim
nj=ydim
nk=zdim
```

```
maxi=xdim1
print *,'allocating...'
allocate(xstore(ni,nj,nk),ystore(ni,nj,nk),zstore(ni,nj,nk))
allocate(x(nk,ni,nj),y(nk,ni,nj),z(nk,ni,nj))
allocate(xr(xdim1,ydim1,zdim1),yr(xdim1,ydim1,zdim1),
& zr(xdim1,ydim1,zdim1))
allocate(xtemp(xdim1,ydim1,zdim1),
& ytemp(xdim1,ydim1,zdim1),ztemp(xdim1,ydim1,zdim1))
allocate(xtemp1(ydim1,xdim1,zdim1),
& ytemp1(ydim1,xdim1,zdim1),ztemp1(ydim1,xdim1,zdim1))
allocate(xfinal(xdim1,ydim1,zdim1),
& yfinal(xdim1,ydim1,zdim1),zfinal(xdim1,ydim1,zdim1))
allocate(rad(ydim))
allocate(leftslope2(ydim))
allocate(rightslope2(ydim))
read(7) (((xstore(i,j,k),i=1,ni),j=1,nj),k=1,nk),
& (((ystore(i,j,k),i=1,ni),j=1,nj),k=1,nk),
& (((zstore(i,j,k),i=1,ni),j=1,nj),k=1,nk)
read(8) (((xr(i,j,k),i=1,xdim1),j=1,ydim1),k=1,zdim1),
& (((yr(i,j,k),i=1,xdim1),j=1,ydim1),k=1,zdim1),
& (((zr(i,j,k),i=1,xdim1),j=1,ydim1),k=1,zdim1)
do i = 1,ni
do j = 1,nj
do k = 1,nk
x(k,i,j) = xstore(i,j,k)
y(k,i,j) = ystore(i,j,k)
z(k,i,j) = zstore(i,j,k)
enddo
enddo
enddo
C Algorithm to find coordinates of the center of the turbine
ni=zdim
nj=xdim
nk=ydim
halfpt = ni/2
leftpty = y(1,1,nk)
leftptz = z(1,1,nk)
centerpty = y(halfpt,1,nk)
centerptz = z(halfpt,1,nk)
```

```
rightpty = y(ni,1,nk)
rightptz = z(ni,1,nk)
bisect1y = (leftpty + centerpty)/2.
bisect1z = (leftptz + centerptz)/2.
bisect2y = (centerpty + rightpty)/2.
bisect2z = (centerptz + rightptz)/2.
leftslope = (centerpty-leftpty)/(centerptz-leftptz)
rightslope = (centerpty-rightpty)/(centerptz-rightptz)
bisect1slope = -1/leftslope
bisect2slope = -1/rightslope
constant1 = bisect1y - bisect1slope*bisect1z
constant2 = bisect2y - bisect2slope*bisect2z
centerz = (constant2-constant1)/(bisect1slope - bisect2slope)
centery = bisect1slope * centerz + constant1
radius = sqrt((leftpty-centery)**2 + (leftptz-centerz)**2)
C End algorithm to find center of the turbine
C Start algorithm to produce temporary exit stator block
do j = 1,nj
if(j>1) then
x(1,j,1) = x(1,j-1,1) + 0.1
y(1,j,1) = y(1,j,1)
z(1,j,1) = z(1,j,1)
endif
do k = 1,nk
rad(k)=sqrt((y(1,1,k)-centery)**2+(z(1,1,k)-centerz)**2)
if(j>1) then
if(k>1) then
x(1,j,k) = x(1,j,1)
y(1,j,k) = sqrt(rad(k)**2-(z(1,j,k)-centerz)**2)+centery
endif
endif
do i = 2,ni
x(i,j,k) = x(1,j,1)
y(i,j,k) = sqrt(rad(k)**2-(z(i,j,k)-centerz)**2)+centery
enddo
enddo
enddo
do j=2,nj
do i=1,ni
```

```
do k=1,nk
z(i,j,k) = z(i,j-1,k)
y(i,j,k) = y(i,j-1,k)
enddo
enddo
enddo
C End algorithm for producing temporary exit stator block
xdim1orig = xdim1
iprime = xdim1
do i = 1,xdim1
do j = 1,ydim1
kprime = zdim1
do k= 1,zdim1
xtemp(i,j,k) = -xr(iprime,j,k)
ytemp(i,j,k) = yr(iprime,j,k)
ztemp(i,j,k) = zr(iprime,j,k)
kprime = kprime - 1
enddo
enddo
iprime = iprime - 1
enddo
do i = 1,xdim1
do j = 1,ydim1
do k= 1,zdim1
xr(i,j,k) = xtemp(i,j,k)
yr(i,j,k) = ytemp(i,j,k)
zr(i,j,k) = ztemp(i,j,k)
enddo
enddo
enddo
C Start algorithm to produce temporary rotor inlet block
C with matching tangential lines to the temporary stator exit block
leftpty1 = yr(xdim1,1,1)
leftptz1 = zr(xdim1,1,1)
rightpty1 = yr(xdim1,1,zdim1)
rightptz1 = zr(xdim1,1,zdim1)
centerpty2 = ABS((leftpty1+rightpty1)/2-rightpty1)
centerptz2 = ABS((leftptz1+rightptz1)/2-leftptz1)
hypot = SQRT((centerpty2*centerpty2)+(centerptz2*centerptz2))
```

```
angle = PI-ATAN(centerptz2/centerpty2)-ATAN(rad(nk)/hypot)
angle = angle*(180/PI)
centerz2 = rightptz1-rad(nk)*sin(angle)
centery2 = rightpty1-rad(nk)*cos(angle)
do j= 1,ydim1
if(j>1) then
xr(1,j,1) = xr(1,j-1,1) - .1
yr(1,j,1) = yr(1,1,1)
endif
do i = 1,xdim1
if(j>1) then
if(i>1) then
xr(i,j,1) = xr(1,j,1)
endif
endif
do k = 1,zdim1
xr(i,j,k) = xr(1,j,1)
enddo
do k = 3,zdim1-5
yr(i,j,k) = sqrt(rad(i)**2-(zr(i,j,k)-centerz)**2)+centery
enddo
enddo
enddo
do j=2,ydim1
do i=1,xdim1
do k=1,zdim1
zr(i,j,k) = zr(i,j-1,k)
yr(i,j,k) = yr(i,j-1,k)
enddo
enddo
enddo
do i = 1,xdim1
do j = 1,ydim1
do k= 1,zdim1
xtemp1(j,i,k) = xr(i,j,k)
ytemp1(j,i,k) = yr(i,j,k)
ztemp1(j,i,k) = zr(i,j,k)
enddo
enddo
```

```
enddo
do i = 1,xdim1
do j = 1,ydim1
do k= 1,zdim1
yfinal(i,j,k) = yr(i,j,k)
zfinal(i,j,k) = zr(i,j,k)
xfinal(i,j,k) = xr(i,j,k)
enddo
enddo
enddo
do j = 1,ydim1
do i = 1,xdim1
halfpt1 = zdim1/2
leftpty1 = yfinal(i,j,1)
leftptz1 = zfinal(i,j,1)
rightpty1 = yfinal(i,j,zdim1)
rightptz1 = zfinal(i,j,zdim1)
centerpty1 = yfinal(i,j,halfpt1)
centerptz1 = zfinal(i,j,halfpt1)
bisect1y1 = (leftpty1 + centerpty1)/2.
bisect1z1 = (leftptz1 + centerptz1)/2.
bisect2y1 = (centerpty1 + rightpty1)/2.
bisect2z1 = (centerptz1 + rightptz1)/2.
leftslope1 = (centerpty1-leftpty1)/(centerptz1-leftptz1)
rightslope1 = (centerpty-rightpty)/(centerptz1-rightptz1)
bisect1slope1 = -1/leftslope1
bisect2slope1 = -1/rightslope1
constant1 = bisect1y1 - bisect1slope1*bisect1z1
constant2 = bisect2y1 - bisect2slope1*bisect2z1
centerz1=(constant2-constant1)/(bisect1slope1-bisect2slope1)
centery1 = bisect1slope1 * centerz1 + constant1
centerpty2 = ABS((leftpty1+rightpty1)/2-rightpty1)
centerptz2 = ABS((leftptz1+rightptz1)/2-leftptz1)
hypot = SQRT((centerpty2*centerpty2)+(centerptz2*centerptz2))
angle = PI-ATAN(centerptz2/centerpty2)-ATAN(rad(nk)/hypot)
angle = angle*(180/PI)
centerz2 = rightptz1-rad(nk)*sin(angle)
centery2 = rightpty1-rad(nk)*cos(angle)
do k = 2,zdim1-1
```

```
zfinal(i,j,k)=zfinal(i,j,k-1)+
& (zfinal(i,j,zdim1)-zfinal(i,j,1))/(zdim1-1)
yfinal(i,j,k)=sqrt(rad(i)**2-
& (zfinal(i,j,k)-centerz)**2)+centery
enddo
C End temporary rotor inlet block algorithm
print *,'start,end:',start,end
enddo
enddo
print *,'writing to stator...'
write(9) (((x(i,j,k),i=1,ni),j=1,nj),k=1,nk),
& (((y(i,j,k),i=1,ni),j=1,nj),k=1,nk),
& (((z(i,j,k),i=1,ni),j=1,nj),k=1,nk)
print *,'writing to temporary rotor....'
write(5) (((xtemp(i,j,k),i=1,xdim1orig),j=1,ydim1),k=1,zdim1),
& (((ytemp(i,j,k),i=1,xdim1orig),j=1,ydim1),k=1,zdim1),
& (((ztemp(i,j,k),i=1,xdim1orig),j=1,ydim1),k=1,zdim1)
print *,'writing to final rotor...'
write(4) (((xfinal(i,j,k),i=1,xdim1),j=1,ydim1),k=1,zdim1),
& (((yfinal(i,j,k),i=1,xdim1),j=1,ydim1),k=1,zdim1),
& (((zfinal(i,j,k),i=1,xdim1),j=1,ydim1),k=1,zdim1)
deallocate(xtemp,ytemp,ztemp)
deallocate(xstore,ystore,zstore)
deallocate(xr,yr,zr)
deallocate(rad)
deallocate(x,y,z)
deallocate(xfinal,yfinal,zfinal)
print *,'closing...'
close(7)
close(9)
close(8)
close(5)
close(6)
end
```

Preprocessor setup

The preprocessor program written by Vikram Shyam takes files produced by GridPro and produces grid files, connectivity files, and boundary condition files necessary for TURBO to run. The following files are required by preprocessor before it can be run:

1. stator grid in gridpro format
2. rotor grid in gridpro format
3. connectivity file from GridPro for stator grid
4. connectivity file from GridPro for rotor grid
5. setup.in

The output of the preprocessor code is the following:

1. GU files
2. bc.in
3. dmap.in
4. turbo.in
5. tasklist.in

GU files are grid files that are in polar coordinates. bc.in contains the boundary condition information for the grid. dmap.in contains the connectivity information. It is a data file of block to block interface connections. turbo.in defines the interfaces for the code as well as the wheel speeds of each blade row. tasklist.in provides the user with the blocks that were manipulated and it gives details on how each one was manipulated.

Setup.in File

```
&SETUP_PARAMS
    num_blade_rows=1
    num_blades=72
    checkconn=1
    conn_tol=0.000000001
    turbo_friendly=.TRUE.
```

row_names=rotor.tmp
/

Parameter	Description
num_blade_rows	number of blade rows
num_blades	Number of blades in each blade row
checkconn	1 = check gridpro connectivity file
conn_tol	Gives a tolerance for inspecting connectivity of gridpoints
turbo_friendly	.TRUE. makes the files ready to be run with MSU-TURBO
row_names	The output names of the finished grids

Table 9.3: Preprocessor setup parameters

Input00 parameters

The following are the input files that MSU-TURBO requires for input parameters. Also, each blade row has its own set of parameters.

Input00 for stator vane case

```
&PARAMETERS
    num_blade_rows = 1
    debug=F
    gofast=T
    /
    &SOLUTION_PARAMETERS
    num_printouts = 2000
    num_iter_per_printout = 10000
    freeze_jacobian = 0
    turbulence_model = 5
    num_iter_restart_write = 100
    max_num_subiter = 2
    temporal_accuracy = 1
    spatial_accuracy = 2
    solution_type = 2
    symmetry_factor = 38
    solution_correct_method = 3
    /
```

```
&INITIAL_CONDITION
initialize_solution = 4
freestream_mach_num=0.0825
/
&REFERENCE_CONDITIONS
ref_pressure = 386934.8673259392
ref_temperature= 627.7112494574653
ref_velocity = 424.4698384740075
ref_length = 0.0254
ref_gamma = 1.3811000585556
gamma_table = 1.3811000585556 1.3811000585556
temp_gam_table = 627.7112494574653 727.7112494574653
gamref_t1 = 1.3811000585556
/
&TIME_SHIFT_BC
use_time_shift_bc=0
initialize_time_shift_in_TURBO=F
time_shift_bc_factor=0.5
/
&INLET_BC
inlet_bc_type=2
/
&EXIT_BC
exit_bc_type=12
back_pressure = 200000.0
/
&KE_MODEL_PARAMETERS
kemdl_input_type = 0
kemdl_init_option = 0
spatial_accuracy_2eq = 3
temporal_accuracy_2eq = 1
inlet_turbulence_intensity = 0.01
inlet_eddy_viscosity = 50.
/
&FLUTTER
/
&WALL_BC
wall_bc_type = 3
wall_temperature = 0.7
```

/
&TIME_STEP
cfl = 5.0
use_local_time_step = 1
num_time_steps_per_period = 1000
omega_ts = 8971.738206257671
num_blds_ts = 38 /
&OUTPUT
output_format=3
num_soln_per_flow_file= 1
num_iter_per_soln_dump= 100
steady_output = T
/
&INLET_PROFILE
span= 0.000000 0.6286892E-01 0.1238000 0.1826010 0.2393550 0.3475620 0.4499890 0.5480280 0.6427300 0.7348540 0.8249240 0.9132630 0.9568270 0.9741390 1.000000
total_pressure= 386932.4 386932.4 386932.4 386932.4 386932.4 386932.4 386932.4 386932.4 386932.4 386932.4 386932.4 386932.4 386932.4 386932.4 386932.4 386932.4
total_temperature= 627.7111 627.7111 627.7111 627.7111 627.7111 627.7111 627.7111 627.7111 627.7111 627.7111 627.7111 627.7111 627.7111 627.7111 627.7111 627.7111
tangential_angle= 0.000000 0.000000 0.000000 0.000000 0.000000 0.000000 0.000000 0.000000 0.000000 0.000000 0.000000 0.000000 0.000000 0.000000 0.000000 0.000000
radial_angle= 20.62260 20.36700 19.92050 19.09590 18.04390 15.62750 13.05410 10.52400 8.125250 5.876350 3.800810 1.948700 1.125790 0.8198330 0.000000
/
&EXIT_PROFILE
span= 0.000000 0.3259316E-01 0.7122011E-01 0.1094400 0.1484380 0.2425160 0.3575400 0.4753630 0.5869790 0.6952940 0.8019380 0.9026380 0.9492640 0.9677140 1.000000
static_pressure= 156540.8 156511.1 157341.3 158163.8 158911.2 161110.6 164753.1 168876.8 172971.6 177185.0 181572.1 185784.8 187754.6 188541.3 189848.5
exit_mass_flow = 11.9
/

Input00 for rotor blade case

&PARAMETERS
num_blade_rows = 1
debug=F

```
gofast=T
/
&SOLUTION_PARAMETERS
num_printouts = 100
num_iter_per_printout = 1000
freeze_jacobian = 0
turbulence_model = 5
max_num_subiter = 2
num_iter_restart_write = 100
temporal_accuracy = 1
spatial_accuracy = 2
solution_type = 2
symmetry_factor=72
solution_correct_method=3
/
&SLIDING_BC
use_conserve_bc = 0
/
&INITIAL_CONDITION
initialize_solution = 4
freestream_mach_num = 0.0
/
&REFERENCE_CONDITIONS
ref_pressure = 386934.8673259392
ref_temperature= 627.7112494574653
ref_velocity = 498.837860498492
ref_length = 0.0254
ref_gamma = 1.3811000585556
gamma_table = 1.3811000585556 1.3811000585556
temp_gam_table = 627.7112494574653 727.7112494574653
gamref_t1 = 1.3811000585556
/
&ke_MODEL_PARAMETERS
kemdl_input_type = 0
kemdl_init_option = 0
spatial_accuracy_2eq = 2
temporal_accuracy_2eq = 1
inlet_turbulence_intensity = 0.01
inlet_eddy_viscosity = 50.
```

/
&TIME_SHIFT_BC
use_time_shift_bc=0
initialize_time_shift_in_TURBO=F
time_shift_bc_factor=0.75
/
&INLET_BC
inlet_bc_type = -2
/
&EXIT_BC
exit_bc_type = 12
back_pressure=80000.0
/
&WALL_BC
wall_bc_type = 3
wall_temperature = 0.7
/
&FLUTTER
/
&TIME_STEP
cfl = 5.0
use_local_time_step = 1
num_time_steps_per_period = 1000
omega_ts = 8971.738206257671
num_blds_ts = 72
/
&OUTPUT
num_soln_per_flow_file = 1
num_iter_per_soln_dump = 300
output_format = 3
steady_output = T
/
&INLET_PROFILE
SPAN =
0.0370 0.1099 0.1830 0.2560
0.3289 0.4019 0.4749 0.5479
0.6208 0.6939 0.7668 0.8398
TOTAL_PRESSURE =
367768.4955 365385.0904 366807.6519 368732.5455

367427.0166 364501.7342 361994.3492 361220.5442
360896.7003 360840.5888 361664.6270 360509.7978
TOTAL_TEMPERATURE =
637.3346 626.8578 628.0498 628.7139
627.9882 627.2383 626.8820 626.9236
626.9340 626.7468 626.9765 627.9527
tangential_angle=
-64.5769 -70.9125 -75.3212 -78.0524
-79.6279 -80.5347 -80.7936 -80.7421
-80.5178 -79.9276 -79.3370 -78.9326
radial_angle=
-7.9150 -8.3771 -9.2108 -9.5294
-9.3194 -8.4889 -7.0741 -5.4284
-3.9708 -2.8020 -1.8646 -0.9503
/
&EXIT_PROFILE
span=
0.0833262 0.1666695 0.2499957 0.3333390
0.4166652 0.5000086 0.5833348 0.6666781
0.7500043 0.8333305 0.9166738 1.000000
static_pressure=
77140.2894 76404.1212 75082.6832 74516.8146
76350.2290 78829.2725 79158.5541 77647.4154
75620.5279 73535.9757 67867.0498 72107.8310
exit_mass_flow = 11.9
/

Input 01 for stator vane simulation

&BLADE_ROW_PARAMETERS
num_blades = 38
omega_bld = 0.0
num_time_steps_stored = -1
num_adjacent_blades = 0
/

Input 01 for rotor blade simulation

&BLADE_ROW_PARAMETERS

num_blades = 72
omega_bld = -8971
num_time_steps_stored= -1
num_adjacent_blades = 0
x_start_hub_rotation = -1
x_end_hub_rotation = 1
/

Procedure for running the steady case in TURBO:

1. Critical input parameters to set before submitting the case.

- Solution_type = 1. The flow should be laminar to start out with. Change this to a value of 2 when convergence between the inlet and exit mass flows are reached.
- Reference pressure = 386934Pa.
- Reference temperature = 627.71 K.
- temporal_accuracy = 1. spatial_accuracy = 1. The flow parameters should be simply calculated to get the flow started. Change spatial_accuracy to 2 later on.
- turbulence_model = 5. This flow will be run with a k-epsilon turbulence model.

2. Critical parameters to reach in order to achieve a converged solution

- Exit pressure profile must be set as the exit boundary condition.
- Mass Flow in the inlet and exit should have less than .1% difference.
- The heat flux should converge. Check the temperature gradient at two iterations of 300. The difference in temperature gradient between these two solutions should be less than 1%.

3. Get exit profile from converged solution for the stator vane and use that profile as the inlet boundary conditions for the rotor blade case. The next section will go into detail as to how to go about doing this.

- omega_blade_ds = -8971. Rotor blade needs to be rotating at a wheel speed 8971 rpm in the counter-clockwise direction.

Block Orientation

The following are the block orientation requirements that need to be satisfied in order for the TURBO computation to be run in a correct manner.

1. K min face must be on the negative periodic boundary surface
2. K max face must be on the positive periodic boundary surface
3. I min face must be at the inlet of the grid
4. I max face must be at the exit of the grid

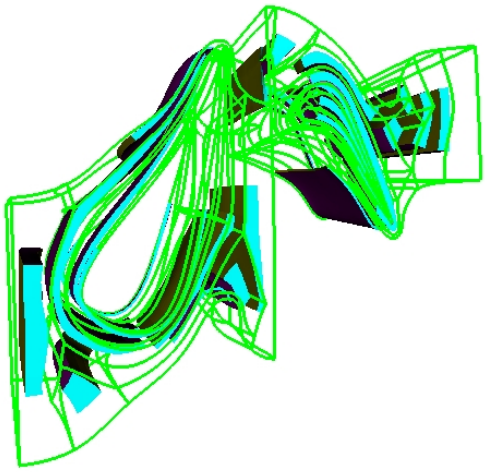

Figure 9.1: Use Gumbo to check block orientation